HHS Public Access

Author manuscript

Neuron. Author manuscript; available in PMC 2019 January 17.

Published in final edited form as:

Neuron. 2018 January 17; 97(2): 313–325.e6. doi:10.1016/j.neuron.2017.12.036.

Epitranscriptomic m^{6}A Regulation of Axon Regeneration in the Adult Mammalian Nervous System

Yi-Lan Weng[1,2], **Xu Wang**[3], **Ran An**[1,2,4], **Jessica Cassin**[5], **Caroline Vissers**[6], **Yuanyuan Liu**[7], **Yajing Liu**[8], **Tianlei Xu**[9], **Xinyuan Wang**[1,10], **Samuel Zheng Hao Wong**[1,11], **Jessica Joseph**[1,11], **Louis C. Dore**[12], **Qiang Dong**[4], **Wei Zheng**[13], **Peng Jin**[14], **Hao Wu**[9], **Bin Shen**[7], **Xiaoxi Zhuang**[15], **Chuan He**[12], **Kai Liu**[3], **Hongjun Song**[1,5,6,11,16,17,18], and **Guo-li Ming**[1,6,11,16,18,19]

[1]Department of Neuroscience, Mahoney Institute for Neurosciences, Perelman School of Medicine, University of Pennsylvania, Philadelphia, PA 19104, USA

[2]Institute for Cell Engineering, Johns Hopkins University School of Medicine, Baltimore, MD 21205, USA

[3]Division of Life Science, State Key Laboratory of Molecular Neuroscience, The Hong Kong University of Science and Technology, Hong Kong, China

[4]Department of Neurology, State Key Laboratory of Medical Neurobiology, Huashan Hospital, Fudan University, Shanghai 200040, China

[5]The Human Genetic Pre-graduate Program, Johns Hopkins University School of Medicine, Baltimore, MD 21205, USA

[6]The Biochemistry, Cellular and Molecular Biology Graduate Program, Johns Hopkins University School of Medicine, Baltimore, MD 21205, USA

[7]State Key Laboratory of Reproductive Medicine, Department of Histology and Embryology, Nanjing Medical University, Nanjing 211166, China

[8]School of Life Science and Technology, ShanghaiTech University, Shanghai, 201210, China

[9]Department of Biostatistics and Bioinformatics, Rollins School of Public Health, Emory University, Atlanta, GA 30322, USA

[10]School of Basic Medical Sciences, Fudan University, Shanghai 200040, China

[19]Lead Contact: gming@pennmedicine.upenn.edu.

AUTHOR CONTRIBUTIONS: Y.L.W. led the project and was involved in all aspects of the study. Xu W., and K.L. performed in vitro neurite outgrowth of DRG neurons and optic nerve injury studies. R.A. performed surgical procedures and data quantification for DRG studies. T.X., P.J. and H.W. helped with some of the bioinformatics analyses, J.C., C.V., Xinyuan W., Z.H.S.W., J.J., Q.D., and W.Z. contributed to other data collection. L.C.D., X.Z. and C.H. provided *Mettl14*$^{f/f}$ mice. Yuanyuan L., Yajing L., B.S., X.Z., and C.H. provided *Ythdf1*$^{-/-}$ mice. Y.L.W., H.S. and G-l.M. designed the project, analyzed the data and wrote the paper. All authors helped prepare the manuscript.

COMPETING FINANCIAL INTERESTS: The authors declare no competing financial interests.

[11]The Cellular and Molecular Medicine Graduate Program, Johns Hopkins University School of Medicine, Baltimore, MD 21205, USA

[12]Department of Chemistry, Institute for Biophysical Dynamics, and Howard Hughes Medical Institute, University of Chicago, Chicago, Illinois 60637, USA

[13]National Center for Advancing Translational Sciences, National Institutes of Health, Bethesda, MD 20892, USA

[14]Department of Human Genetics, School of Medicine, Emory University, Atlanta, GA 30322, USA

[15]Department of Neurobiology, University of Chicago, Chicago, Illinois 60637, USA

[16]Department of Cell and Developmental Biology, Perelman School of Medicine, University of Pennsylvania, Philadelphia, PA 19104, USA

[17]The Epigenetics Institute, Perelman School of Medicine, University of Pennsylvania, Philadelphia, PA 19104, USA

[18]Institute for Regenerative Medicine, Perelman School of Medicine, University of Pennsylvania, Philadelphia, PA 19104, USA

SUMMARY

N^6-methyladenosine (m^6A) affects multiple aspects of mRNA metabolism and regulates developmental transitions by promoting mRNA decay. Little is known about the role of m^6A in the adult mammalian nervous system. Here we report that sciatic nerve lesion elevates levels of m^6A-tagged transcripts encoding many regeneration-associated genes and protein translation machinery components in the adult mouse dorsal root ganglion (DRG). Single-base resolution m^6A-CLIP mapping further reveals a dynamic m^6A landscape in the adult DRG upon injury. Loss of either m^6A methyltransferase complex component Mettl14, or m^6A-binding protein Ythdf1, globally attenuates injury-induced protein translation in adult DRGs and reduces functional axon regeneration in the peripheral nervous system in vivo. Furthermore, *Pten* deletion-induced axon regeneration of retinal ganglion neurons in the adult central nervous system is attenuated upon *Mettl14* knockdown. Our study reveals a critical epitranscriptomic mechanism in promoting injury-induced protein synthesis and axon regeneration in the adult mammalian nervous system.

ETOC

N^6-methyladenosine (m^6A) occurs in many mRNAs. Weng et al. uncovered an epitranscriptomic mechanism wherein axonal injury elevates m^6A levels and signaling to promote protein translation, including regeneration-associated genes, which is essential for functional axon regeneration of peripheral sensory neurons.

INTRODUCTION

Studies in the past few years have revealed various dynamic modifications of mRNA, including N^6-methyladenosine (m^6A), N^1-methyladenosine (m^1A), 5-methylcytosine (m^5C), and pseudouridine (ψ) (Gilbert et al., 2016; Li et al., 2016; Zhao et al., 2017a). Among these

modifications, m^6A is the most abundant internal modification of mRNA in eukaryotic cells (Desrosiers et al., 1975). m^6A sites are present in over 25% of human transcripts, with enrichment in long exons, and near transcription start sites and stop codons (Dominissini et al., 2012; Ke et al., 2015; Meyer et al., 2012). Almost every gene produces both methylated and unmethylated transcripts, highlighting the highly complex and heterogeneous nature of transcriptomes (Molinie et al., 2016). So far, m^6A profiling analyses have been performed mostly with cell lines and bulk tissues due to the requirement of a substantial amount of input mRNA (Li et al., 2016). In part due to this technical limitation, the m^6A landscape and its temporal and spatial dynamics in specific regions of the mammalian nervous system in vivo remain largely unknown.

In mammals, m^6A is installed by a methyltransferase complex consisting of Mettl3, Mettl14, and other components, and can be removed by demethylases Fto and Alkbh5 (Wang et al., 2017; Zhao et al., 2017a). Recent studies have implicated m^6A in regulating mRNA processing in the nucleus, and translation and decay in the cytoplasm (Zhao et al., 2017a). These different functions of m^6A modifications are believed to be mediated by diverse m^6A-binding proteins, such as YT521-B homology domain family (YTHDF) proteins (Zhao et al., 2017a). For example, in vitro studies in cell lines have suggested that m^6A promotes protein translation efficacy via YTHDF1 and YTHDF3, and promotes mRNA decay via YTHDF2 (Li et al., 2017a; Lin et al., 2016; Meyer et al., 2015; Shi et al., 2017; Wang et al., 2015; Zhou et al., 2015). Functionally, m^6A regulates self-renewal and differentiation of mouse embryonic stem cells and glioblastoma stem cells in vitro by promoting mRNA decay (Batista et al., 2014; Cui et al., 2017; Geula et al., 2015; Wang et al., 2014). During development, m^6A regulates sex determination and neuronal functions by modulating mRNA splicing in *Drosophila* (Haussmann et al., 2016; Lence et al., 2016) and maternal-to-zygotic transition via Ythdf2-mediated maternal mRNA clearance in *Zebrafish* (Zhao et al., 2017b). More recent in vivo studies of embryonic mouse development have revealed deficits in stem cell self-renewal and differentiation in the blood and nervous systems (Li et al., 2017b; Yoon et al., 2017; Zhang et al., 2017). These studies have established critical roles for m^6A-dependent mRNA decay in regulating developmental transitions (Zhao et al., 2017a). The role of m^6A in the adult mammalian nervous system under physiological and pathological conditions remains largely unexplored.

Sensory neurons in the adult mouse dorsal root ganglion (DRG) exhibit robust axon regeneration in the peripheral nervous system (PNS) through a process involving de novo gene transcription and protein synthesis of regeneration-association genes (RAGs) (Costigan et al., 2002; Moore and Goldberg, 2011; Smith and Skene, 1997). Axon regeneration can also be induced in the adult central nervous system (CNS), for example, by *Pten* deletion in retinal ganglion neurons and corticospinal neurons (Liu et al., 2010; Park et al., 2008). Previous studies have identified transcriptional mechanisms that promote intrinsic axon growth capacity (Liu et al., 2011; Moore and Goldberg, 2011; Tedeschi and Bradke, 2016). More recently, epigenetic mechanisms, including both histone acetylation (Cho et al., 2013; Finelli et al., 2013; Gaub et al., 2011; Puttagunta et al., 2014) and DNA methylation (Weng et al., 2017), have been shown to promote transcriptional activation of multiple RAGs, and are required for robust axon regeneration of adult mouse DRG neurons upon peripheral nerve injury (Weng et al., 2013; Weng et al., 2016). The discovery of widespread m^6A

modification and its potential roles in regulating RNA metabolism (Gilbert et al., 2016; Li et al., 2016; Zhao et al., 2017a) raises the question of whether an epitranscriptomic mechanism may contribute to axon regeneration in the adult mammalian nervous system. Here we investigated the potential role and mechanism of m^6A methylation in regulating injury responses and axon regeneration in the adult mouse PNS and CNS.

RESULTS

Peripheral Axon Injury Elevates m^6A-tagged Transcript Levels

Using a mouse line that specifically labels DRG neurons (Kim et al., 2016) and glutamine synthetase as a marker for surrounding satellite glia, we found that m^6A was present mostly in neurons within the adult DRGs (Figure S1A). Furthermore, peripheral sciatic nerve lesion (SNL) elevated m^6A levels in adult DRG neurons, reaching a peak around days 1 to 3 (D1-3) and then gradually returning back to the basal level (Figure S1A–C). We next performed genome-wide profiling of m^6A-tagged mRNA in the adult DRG under naïve and SNL D1 conditions. To overcome limited mRNA input from L4/L5 DRGs of adult mice, we adapted a m^6A-seq method using the SMART2-seq technology, which has recently been used to linearly amplify transcripts for single-cell RNA-seq (Picelli et al., 2014) (named m^6A-SMART-seq; Figure S1D–E). Since the same gene could produce both m^6A-tagged and untagged transcripts (Molinie et al., 2016), we applied a statistical approach to identify genes for which a substantial proportion of total transcripts was m^6A-tagged (Figure S1F and Table S1). The majority of genes with substantial m^6A-tagging was shared between naïve and SNL D1 conditions (Figure 1A). Interestingly, 129 of 304 known RAGs (Chandran et al., 2016) exhibit significant m^6A-tagging at SNL D1 (Figure 1B; $P <$ 4.550e-07; hypergeometric test).

We next performed a quantitative comparison of m^6A-tagged mRNA levels between naïve and SNL D1 conditions. A total of 182 m^6A-tagged genes were substantially upregulated, while few were downregulated (fold change ≥ 2; Figure 1C and Table S2). Therefore, consistent with m^6A immunostaining results (Figure S1A–C), peripheral nerve injury mostly elevates m^6A-tagged transcript levels. Notably, 30 RAGs, including *Atf3* (Fagoe et al., 2015; Seijffers et al., 2007), *Sox11* (Jankowski et al., 2009), *Gadd45a* (Befort et al., 2003), and *Tet3* (Weng et al., 2017), exhibited increased levels of m^6A-tagged transcripts at SNL D1 (Figure 1C–D). We validated our m^6A-SMART-seq results for a select group of RAGs using m^6A-MeRIP Q-PCR analysis of independent biological samples (Figure 1E and Table S3).

We further performed nonbiased Gene Ontology (GO) analysis for upregulated m^6A-tagged transcripts. Notably, the most enriched biological term was translation, followed by metabolism-related process (Figure 1F). For example, many transcripts encoding ribosomal subunit proteins, such as *Rps14, Rps20, Rps23, Rps28* and *Rps29*, and eukaryotic initiation factors, such as *Eif1a* and *Eif3b*, exhibited elevated levels of m^6A-tagged transcripts at SNL D1 (Figure 1D).

For a given gene, an increase in the m^6A-tagged transcript level could be due to elevated total transcript levels without changes in the proportion of tagged transcripts, or increased tagging with or without affecting the total transcript level. Therefore, we compared fold

changes in m^{6}A-tagged and total transcript levels between naïve and SNL D1 conditions. The majority of RAGs, such as *Atf3*, *Sox11*, and *Jun*, exhibited a correlated increase in both m^{6}A-tagged and total transcript levels upon SNL, whereas most ribosomal subunit genes with increased m^{6}A-tagged transcript levels did not alter their total transcript levels (Figure 1G). Taken together, these quantitative analyses reveal that peripheral nerve injury mostly up-regulates m^{6}A levels in DRGs with an enrichment of transcripts related to RAGs and protein translation machinery, involving both transcription activation-coupled m^{6}A methylation and an increased proportion of m^{6}A-tagged transcript levels without transcription upregulation.

Single-base m^{6}A Mapping Reveals a Dynamic m^{6}A Landscape in Response to Injury

While our m^{6}A-SMART-seq approach can quantify the amount of m^{6}A-tagged transcripts, it does not identify the location of m^{6}A sites within transcripts. We next performed m^{6}A-CLIP-seq, which provides single-base resolution mapping of m^{6}A across the transcriptome (Linder et al., 2015). Similarly, we adapted the SMART2-seq technology to overcome the small amount of mRNA input from L4/L5 DRGs (named m^{6}A-CLIP-SMART-seq; Figure S2A–B and Table S4). Under both naïve and SNL D1 conditions, we identified m^{6}A sites enriched in exons and near transcription start sites and stop codons across transcriptomes (Figure S2C–D), which is similar to previous findings from cell lines (Linder et al., 2015).

Consistent with our m^{6}A-SMART-seq results (Figure 1A), m^{6}A-CLIP-SMART-seq showed that the majority of m^{6}A-tagged transcripts was shared between naïve and SNL D1 conditions (Figure 2A). Notably, there were dynamic changes in m^{6}A sites (Figure 2B). Some transcripts exhibited a gain and/or loss of m^{6}A sites across the 5′ UTR, coding regions, and 3′ UTR, whereas other transcripts displayed region-specific changes (Figure 2B and Table S5). Multiple RAGs, such as *Atf3* and *Tet3*, gained new m^{6}A sites upon SNL (Figure 2C). Notably, transcripts encoding retrograde injury signaling molecules, such as Vimentin (Vim) (Perlson et al., 2005), exhibited dynamic m^{6}A sites upon SNL (Figure 2C). In general, RAG transcripts exhibited a larger gain in m^{6}A sites compared to non-RAG transcripts and new sites were located mostly in coding regions, whereas ribosomal subunit-related genes exhibited a similar gain in m^{6}A sites as other genes (Figure 2D). Across the transcriptome, GO analysis showed that transcripts with newly added m^{6}A sites were enriched for axonal regulation, whereas transcripts with a loss of m^{6}A sites were enriched for presynaptic functions of neurons (Figure 2E).

We next cross-compared m^{6}A-seq and m^{6}A-CLIP-seq datasets. While many RAGs exhibited increased m^{6}A-tagged transcripts and gained new m^{6}A sites, most transcripts encoding protein translation machinery components showed increased m^{6}A-tagged transcript levels, but not new m^{6}A sites (Figure S2E). Together, our quantitative and single-base m^{6}A mapping reveals a dynamic landscape of mRNA methylation in adult DRGs in response to injury.

Mettl14 Regulates Injury-induced de novo Protein Synthesis

To determine the function of m^{6}A in the adult DRG, we examined conditional knockout mice of *Mettl14* (Yoon et al., 2017), a core subunit of the mammalian m^{6}A

methyltransferase complex (Wang et al., 2017). We deleted *Mettl14* specifically in post-mitotic neurons in vivo using the *Syn1-Cre; Mettl14*$^{f/f}$ (cKO) model. We confirmed *Mettl14* deletion in adult DRGs at the protein level by Western blot (Figure S3A). Quantitative dot blot analysis showed largely diminished m^{6}A levels in purified mRNA from cKO DRGs compared to wildtype (WT) littermates (Figure 3A).

m^{6}A methylation has been implicated in regulating both mRNA decay and protein translation of tagged transcripts (Zhao et al., 2017a). To examine the potential impact of m^{6}A on total mRNA levels, we performed RNA-seq analysis of adult DRGs from WT and *Mettl14* cKO mice under both naïve and SNL D1 conditions (Table S6). We found very similar gene expression profiles between WT and cKO DRGs, under both naïve and injury conditions (Figure S3B). For RAGs, we also observed similar induction in WT and cKO DRGs (Figure 3B). Therefore, the impact of m^{6}A methylation on total transcript levels appears to be minimal under our experimental conditions.

We next examined the effect of *Mettl14* deletion on protein translation in the adult DRG. We employed the SUnSET assay in vivo to label nascent proteins with puromycin (Goodman et al., 2011; Schmidt et al., 2009) (Figure S3C). Analysis of WT adult DRGs showed a global increase of new protein synthesis at SNL D1 (Figure 3C–D and S3D), indicating that peripheral nerve lesion promotes protein translation in the cell body as part of the injury response. In *Mettl14* cKO DRGs, SNL-induced protein synthesis was significantly reduced globally compared to WT DRGs, whereas the basal level under the naïve condition was similar to WT (Figure 3C–D and S3D). To validate our result using an independent approach, we examined *Atf3*, one of the most robustly induced genes by SNL, which has been shown to enhance peripheral nerve regeneration by increasing the intrinsic growth competence of adult DRG neurons (Fagoe et al., 2015; Seijffers et al., 2007). The *Atf3* mRNA was also induced in *Mettl14* cKO DRGs, although at a lower level compared to WT at SNL D1 (Figure S3E). We confirmed the loss of m^{6}A methylation in *Atf3* mRNA in *Mettl14* cKO DRGs (Figure S3F). Immunostaining showed little ATF3 protein expression under the naïve condition, in contrast to robust induction at SNL D1 in WT adult DRGs (Figure 3E–F). This induction was drastically reduced in *Mettl14* cKO DRGs at SNL D1 (Figure 3E–F). Using quantitative Western blot analysis, further time course analysis showed a delayed induction of ATF3 protein in *Mettl14* cKO DRGs (Figure 3G–H). Together, these results indicate that Mettl14-mediated m^{6}A methylation is critical for SNL-induced protein translation in adult DRGs in vivo, which is known to promote axon regeneration of mature mammalian neurons (Abe et al., 2010).

Mettl14 is Required for Robust DRG Neuron Axon Regeneration and Behavioral Recovery

We next directly examined the functional role of *Mettl14* on axon regeneration of DRG neurons after injury. We first used an in vitro neurite outgrowth assay with primary neurons from adult mouse DRGs (Chen et al., 2016). Cultures were infected with AAV2 to express the shRNA against *Mettl14* (Wang et al., 2014), followed by re-plating to mimic axotomy. We found that expression of shRNA-Mettl14 reduced the length of the longest neuronal process of each neuron compared to expression of shRNA-control, indicating an important role of Mettl14 in axon regeneration of DRG neurons (Figure S4A–B).

We next assessed the in vivo role of Mettl14 in functional axon regeneration of adult DRG neurons after SNL. To avoid potential complications of *Mettl14* deletion on DRG neuronal development and maturation in the *Syn1-Cre;Mettl14*$^{f/f}$ cKO model, we instead infected L4/L5 DRGs in adult *Mettl14*$^{f/f}$ mice via targeted intrathecal injection of AAV2/9 expressing Cre (Weng et al., 2017). This approach leads to infection of over 70% of all neurons, but not surrounding satellite glia, in L4/5 DRGs (Figure S4C) (Weng et al., 2017). Regenerating sensory axons were identified by SCG10 immunostaining at SNL D3 (Shin et al., 2014). We found that extension of SCG10^{+} axons was substantially decreased in AAV-Cre;*Mettl14* cKO mice compared to WT littermates (Figure 4AB). Similar results were obtained from the *Syn1-Cre;Mettl14*$^{f/f}$ cKO model (Figure S4D–E). We observed minimal cleaved-caspase 3 expression in the adult DRG upon SNL, indicating that cell death is not a major factor under these conditions (Figure S4F).

Regenerating axons of sciatic nerves extend to the epidermis and start to re-innervate the skin of the hind paw around 2-3 weeks after injury (Weng et al., 2017). Analysis of skin biopsies showed no PGP9.5^{+} sensory axon innervation to the epidermis of the hind paw at SNL D7, indicating effective degeneration of pre-existing mature axons of both WT and AAV-Cre;*Mettl14* cKO DRG neurons (Figure S4G). At SNL D21, innervation to all three epidermal zones by regenerating axons in adult AAV-Cre;*Mettl14* cKO mice was significantly reduced compared to those in WT mice, but no difference was observed under the naïve condition (Figure 4C–D).

To further assess the functional outcome on axon regeneration, we performed a behavioral test to quantify the latency of heat-evoked hind paw withdrawal (Wright et al., 2014). Both WT and AAV-Cre;*Mettl14* cKO animals exhibited similar response latencies to a radiant thermal stimulus at SNL D1 and D7 (Figure 4E). Starting from SNL D18, the withdrawal latency gradually recovered in the WT group, but only minimally recovered in *Mettl14* cKO animals (Figure 4E). Together, these results indicate an essential role of m^{6}A mRNA methylation in functional sensory axon regeneration of adult DRG neurons in vivo.

YTHDF1 is Required for SNL-induced Global Protein Synthesis and Robust Axon Regeneration of DRG Neurons

To further support our model that m^{6}A signaling promotes global protein synthesis and axon regeneration upon injury and to investigate the downstream mechanism, we examined the KO mice of *Ythdf1* (Figure S5A), an m^{6}A reader that has been implicated in promoting protein translation efficacy of m^{6}A-tagged transcripts in cell lines (Shi et al., 2017; Wang et al., 2015). Q-PCR analysis showed similar induction of RAGs at mRNA levels in WT and *Ythdf1* KO adult DRGs (Figure S5B). In contrast, the SUnSET assay revealed a marked reduction of SNL-induced global de novo protein synthesis in adult DRGs of *Ythdf1* KO mice (Figure 5A–B and S5C). Similar to *Mettl14* deletion, the extension of regenerating SCG10^{+} axons was substantially reduced in *Ythdf1* KO mice compared to WT mice at SNL D3 (Figure 5C–D). We observed minimal cleaved-caspase 3 expression in the adult DRG in WT and *Ythdf1* cKO mice upon SNL (Figure S5D). Together, these results further support our model and identify YTHDF1 as a key player in promoting injury-induced protein translation and axon regeneration of adult DRGs in vivo.

Mettl14 is Required for *Pten* Deletion-induced Robust Axon Regeneration of Adult Retinal Ganglion Neurons

Finally, we assessed whether m^6A signaling is also involved in axon regeneration in the adult CNS. We employed the model of *Pten* deletion-induced axon regeneration of retinal ganglion cells (RGCs) in adult mice (Park et al., 2008). We co-expressed Cre and shRNA-Mettl14 in adult RGCs by AAV, followed by axotomy, axonal labeling and analysis in *Pten* cKO or WT mice (Park et al., 2008). Expression of shRNA-Mettl14 alone did not lead to any axon regeneration of RGCs (Figure S6A), but markedly attenuated *Pten* deletion-induced regeneration compared to shRNA-control (Figure 6A–B). The ratio of phospho-$S6^+$ RGCs remained the same between expression of shRNA-control and shRNA-Mettl14 in *Pten* cKO mice (Figure 6C–D), suggesting that blockage of axon regeneration is not likely to be due to the inactivation of mTOR signaling. Notably, there was a 35.1% reduction in the number of $Tuj1^+$ RGCs upon *Mettl14* knockdown in the *Pten* cKO mice, but not in the WT mice (Figure 6D and S6B–C), suggesting that Mettl14 is also involved in *Pten* deletion-induced survival of RGCs. There was a larger decrease in the number of regenerating axons at all distances examined (53.3% reduction on average; Figure 6B), indicating that the survival effect alone could not explain the impact of Mettl14 knockdown on axon regeneration in *Pten* cKO mice. Previous studies have shown that survival rates varied dramatically among neuronal subtypes in the adult retina, with $SMI32^+$ alpha-RGCs (αRGCs) surviving preferentially and accounting for nearly all axon regeneration following *Pten* deletion (Duan et al., 2015). We found that the percentage of αRGCs among surviving $Tuj1^+$ RGCs was not affected by *Mettl14* knockdown in *Pten* cKO mice (Figure S6D). Together, these result suggest that Mettl14 promotes both survival and axonal extension of $Pten^{-/-}$ RGCs after injury in the adult CNS.

DISCUSSION

Our study reveals a critical role of m^6A epitranscriptomic regulation in injury responses and functional axon regeneration in the adult mammalian nervous system in vivo. De novo gene transcription and protein translation are known to be required for robust axon regeneration of adult neurons upon injury and previous studies have identified important roles of transcriptional and epigenetic mechanisms, including both histone and DNA modifications (Cho and Cavalli, 2014; Trakhtenberg and Goldberg, 2012; Weng et al., 2016; Wong and Zou, 2014). Our study reveals another layer of regulation and suggests a model wherein PNS injury elevates methylated mRNA transcripts, including RAGs, which are then subjected to enhanced protein translation for effective axon regeneration. The finding that some epigenetic regulators, such as *Tet3 and Gadd45* (Guo et al., 2011; Yao et al., 2016), are m^6A-tagged, suggests a potential interaction between epigenetic and epitranscriptomic pathways. Our initial study also suggests a similar role of m^6A epitranscriptomic regulation of induced axon regeneration in the adult mammalian CNS.

Mechanistically, our study provides in vivo evidence for a critical role of m^6A in promoting protein translation in the mammalian system. Different from previous findings on the in vivo role of m^6A-dependent promotion of mRNA decay in regulating embryonic development (Li et al., 2017b; Yoon et al., 2017; Zhang et al., 2017; Zhao et al., 2017b), the impact of m^6A

methylation on total mRNA levels appears to be minimal in adult mouse DRGs under both basal and injury conditions. Instead, m^6A plays a critical role in peripheral nerve injury-induced global protein translation in adult mouse DRGs in vivo via YTHDF1. De novo protein synthesis is known to be critical for axon regeneration in the adult mammalian PNS and CNS (Belin et al., 2015; Cho et al., 2015; Donnelly et al., 2013; Jung et al., 2012; Rishal and Fainzilber, 2014; Song and Poo, 2001; van Niekerk et al., 2016). We have identified three classes of transcripts with substantial m^6A-tagging. First, many transcripts encoding RAGs exhibit elevated m^6A levels and new m^6A sites upon SNL. Second, some retrograde injury signaling molecules exhibit m^6A-tagging and increased m^6A sites upon SNL. This result raises the possibility that m^6A-tagging may promote local protein translation to enhance retrograde signaling upon injury, which is known to be required for robust axonal regeneration of DRG neurons (Rishal and Fainzilber, 2014). Third, many transcripts encoding the molecular machinery for protein translation, including both ribosomal subunits and initial complex components, are themselves m^6A-tagged. Therefore, injury may promote global protein translation by augmenting the general translation machinery. Together, this injury-induced reconfiguration of the epitranscriptome may prioritize mechanisms to synthesize critical factors and rapidly turn on the regenerative program. How the specificity of dynamic m^6A modification arises is an important question for future investigation. Our detailed analysis of ATF3 in *Mett14* cKO mice showed a delayed induction at the protein level (Figure 3G–H), yet functional axon regeneration did not recover (Figure 4E). It is likely that injury induces a coordinated response with a cascade of de novo gene expression and protein synthesis. We thus propose a model wherein m^6A methylation is critical for the coordination of new protein synthesis in injury responses, deficits of which lead to defective axon regeneration and functional recovery.

Typically, MeRIP-seq and HITS-CLIP-seq have been used for m^6A or protein-RNA interaction profiling. One major technical limitation of these methods is that the library preparation normally requires a large amount of starting material and the process involves multiple tedious steps. To overcome limitations imposed on the quantity of source material imposed by the small number of axotomized DRGs, we developed new methods for library construction to quantify m^6A-tagged transcript levels and identify m^6A locations. Our approach not only utilizes a template-switching mechanism to avoid effects of ligation bias, but also substantially increases the sensitivity and shortens the processing time. These techniques will allow analyses of epitranscriptomes, including m^6A, m^1A and potentially other mRNA modifications, in a tissue-specific manner.

m^6A levels increase over development in the mouse nervous system (Meyer et al., 2012) and can be dynamically regulated via active demethylation (Jia et al., 2011; Zheng et al., 2013). Recent studies of the m^6A demethylase Fto have revealed its critical roles in regulating adult neurogenesis (Li et al., 2017c), memory formation and consolidation (Walters et al., 2017; Widagdo et al., 2016), and local axonal protein translation (Yu et al., 2017). Together with these studies, our findings suggest that m^6A mRNA methylation may play a broader role in normal physiology and responses to pathological stimuli in the adult mammalian nervous system.

STAR METHODS

KEY RESOURCES TABLE

REAGENT or RESOURCE	SOURCE	IDENTIFIER
Antibodies		
Mouse anti-Puromycin	Millipore	MABE343; RRID:AB_2566826
Rabbit anti-ATF3	Santa Cruz	sc-188; RRID:AB_2258513
Rabbit anti-PGP9.5	AbD Serotec	7863-0504; RRID:AB_2210505
Rabbit anti-SCG10	Novus Biologicals	NBP1-49461; RRID:AB_10011569
Rabbit anti-m6A	Synaptic systems	202003; RRID:AB_2279214
Rabbit anti-Mettl14	Proteintech	26158-1-AP; N/A
Rabbit anti-cleaved caspase 3	Invitrogen	9H19L2; RRID:AB_2532293
Rabbit anti-GAPDH	Abcam	Ab9485; RRID:AB_307275
Mouse anti-GAPDH	EMD Millipore	AB2302; RRID:AB_10615768
Rabbit anti-YTHDF1	Proteintech	17479-1-AP; RRID:AB_2217473
Rabbit anti-pS6	Cell Signaling	4858; RRID:AB_916156
Mouse anti-SMI32	BioLegend	801701; RRID:AB_2564642
Mouse anti-Tuj1	BioLegend	801202; RRID:AB_10063408
Mouse anti-Glutamine Synthetase	Santa Cruz	sc-74430; RRID:AB_1127501
Cy2–, Cy3– or Cy5–conjugated secondary antibodies	Jackson ImmunoResearch	705-225-147; RRID:AB_2307341 711-165-152; RRID:AB_2307443 715-175-150; RRID:AB_2340819
HRP-conjugated goat anti-mouse IgG	Santa Cruz	sc-2031; RRID:AB_631737
HRP-conjugated goat anti-rabbit IgG	Santa Cruz	sc-2004; RRID:AB_631746
Biological Samples		
Chemicals, Peptides, and Recombinant Proteins		
TRIzol	Thermo Fisher	15596018
Formaldehyde	Sigma-Aldrich	F8775-25ML
N^6-Methyladenosine	Sigma-Aldrich	M2780
Puromycin Dihydrochloride	Sigma-Aldrich	P8833-25MG
Cholera Toxin B Subunit, FITC Conjugate	Sigma-Aldrich	C1655-5MG
Fluoro-Max fluorescent beads	Invitrogen	B0100
Critical Commercial Assays		
Collagenase	Invitrogen	17100017
Zamboni's fixative	Newcomer Supply	1459
RNA fragmentation reagents	Thermo Fisher	AM8740
RNA clean and concentrator	Zymo Research	R1017
SMARTScribe reverse transcriptase	Clontech	639537
SuperSignal West Dura Extended Duration Substrate	Thermo Fisher	34075
Protein A Dynabeads	Thermo Fisher	10002D
Fast SYBR Green Master Mix	ABI	4385612
FastAP	Thermo Fisher	EF0651
E. coli Poly(A) Polymerase	NEB	M0276S
Proteinase K	Thermo Fisher	25530049
SUPERase In RNase Inhibitor	Thermo Fisher	AM2696
mMessage mMachine T7 Ultra kit	ThermoFisher	AM1345
Dynabeads Oligo $(dT)_{25}$	ThermoFisher	61006
SMARTScribe reverse transcriptase	Clontech	639537
Advantage 2 Polymerase Mix	Clontech	639201

REAGENT or RESOURCE	SOURCE	IDENTIFIER
KAPA HiFi PCR Kits	Kapa Biosystems	KK2502
Agencourt AMPure XP	Beckman Coulter	A63880
EZ-Tn5 Transposase	Epicentre	TNP92110
Rabbit IgG	Cell Signaling	2729
Deposited Data		
Raw and analyzed data	This paper	GSE106423
Experimental Models: Cell Lines		
Experimental Models: Organisms/Strains		
Mouse: Adult C57Bl6/J	Charles River	N/A
Mouse: *Mettl14*$^{fl/fl}$ C57Bl6/J	Yoon et al., 2017	N/A
Mouse: *Ythdf1*$^{-/-}$ C57Bl6/J	C.H., in preparation	N/A
Mouse: *Pten*$^{f/f}$ mice C57Bl6/J	Park et al., 2008	N/A
Mouse: *Pirt-GCaMP3* C57Bl6/J	Weng et al., 2017	N/A
Mouse: *Synapsin1-Cre*	Charles River	N/A
Recombinant DNA		
AAV2/9 virus	Guo et al., 2011b	N/A
AAV2 virus	Weng et al. 2017	N/A
AAV2/9 GFP-Cre virus	UPenn Vector Core	V1656
Sequence-Based Reagents		
qPCR primers	This paper	See Table S5
Control shRNA: CCTAAGGTTAAGTCGCCCTC	Wang, Y. et al. 2014	N/A
Mettl14 shRNA: GCATTGGTGCTGTGTTAAATA	Wany, Y. et al. 2014	N/A
Software and Algorithms		
NeuronJ	Meijering et al., 2004	RRID:SCR_002074; https://imagescience.org/meijering/software/neuronj/
Image J	NIH	RRID:SCR_003070; https://imagej.nih.gov/ij/
STAR	Dobin, A., 2013	RRID:SCR_005622; https://github.com/alexdobin/STAR
CIMS	Zhang, C., 2011	https://github.com/chaolinzhanglab/ctk/tree/v1.0.3
Trimmomatic	Bolger, A.M., 2014	RRID:SCR_011848; http://www.usadellab.org/cms/?page=trimmomatic
Samtools	Li, H., 2009	RRID:SCR_002105;http://samtools.sourceforge.net/
Bedtools	Quinlan, A.Q., 2010	RRID:SCR_006646; http://bedtools.readthedocs.io/en/latest/
Other		
30 gauge syringe	Hamilton	
Ultra-fine hemostatic forceps	F.S.T.	13021-12
Radiant heat light source (model 33 Analgesia Meter)	IITC/Life Science Instruments	
Confocal Microscope	Zeiss	
Applied Biosystems 7500	ThermoFisher	
Dumont number 5 forceps	Roboz	
Hybond-N+ membrane	GE Healthcare	RPN2020N
UV stratalinker 1800	Stratagene	
10% Mini-PROTEAN® TGX™ Precast Protein Gels	Bio-rad	4561033
Trans-Blot® Turbo™ Mini PVDF Transfer Packs	Bio-rad	1704156
Trans-Blot® Turbo™ Transfer Starter System	Bio-rad	1704155
Dounce tissue grinder set	Sigma	D9938-1SET
Bioruptor plus	Diagenode	

TABLE WITH EXAMPLES FOR AUTHOR REFERENCE

REAGENT or RESOURCE	SOURCE	IDENTIFIER
Antibodies		
Rabbit monoclonal anti-Snail	Cell Signaling Technology	Cat#3879S; RRID: AB_2255011
Mouse monoclonal anti-Tubulin (clone DM1A)	Sigma-Aldrich	Cat#T9026; RRID: AB_477593
Rabbit polyclonal anti-BMAL1	This paper	N/A
Biological Samples		
Healthy adult BA9 brain tissue	University of Maryland Brain & Tissue Bank; http://medschool.umaryland.edu/btbank/	Cat#UMB1455
Human hippocampal brain blocks	New York Brain Bank	http://nybb.hs.columbia.edu/
Patient-derived xenografts (PDX)	Children's Oncology Group Cell Culture and Xenograft Repository	http://cogcell.org/
Chemicals, Peptides, and Recombinant Proteins		
MK-2206 AKT inhibitor	Selleck Chemicals	S1078; CAS: 1032350-13-2
SB-505124	Sigma-Aldrich	S4696; CAS: 694433-59-5 (free base)
Picrotoxin	Sigma-Aldrich	P1675; CAS: 124-87-8
Human TGF-β	R&D	240-B; GenPept: P01137
Activated S6K1	Millipore	Cat#14-486
GST-BMAL1	Novus	Cat#H00000406-P01
Critical Commercial Assays		
EasyTag EXPRESS 35S Protein Labeling Kit	Perkin-Elmer	NEG772014MC
CaspaseGlo 3/7	Promega	G8090
TruSeq ChIP Sample Prep Kit	Illumina	IP-202-1012
Deposited Data		
Raw and analyzed data	This paper	GEO: GSE63473
B-RAF RBD (apo) structure	This paper	PDB: 5J17
Human reference genome NCBI build 37, GRCh37	Genome Reference Consortium	http://www.ncbi.nlm.nih.gov/projects/genome/assembly/grc/human/
Experimental Models: Cell Lines		
Hamster: CHO cells	ATCC	CRL-11268
D. melanogaster: Cell line S2: S2-DRSC	Laboratory of Norbert Perrimon	FlyBase: FBtc0000181
Human: Passage 40 H9 ES cells	MSKCC stem cell core facility	N/A
Human: HUES 8 hESC line (NIH approval number NIHhESC-09-0021)	HSCI iPS Core	hES Cell Line: HUES-8
Experimental Models: Organisms/Strains		
Streptococcus pyogenes: M1 serotype strain: strain SF370; M1 GAS	ATCC	ATCC:700294
C. elegans: Strain BC4011: srl-1(s2500) II; dpy-18(e364) III; unc-46(e177)rol-3(s1040) V.	Caenorhabditis Genetics Center	WB Strain: BC4011; WormBase: WBVar00241916
D. melanogaster: RNAi of Sxl: y[1] sc[*] v[1]; P{TRiP.HMS00609}attP2	Bloomington Drosophila Stock Center	BDSC:34393; FlyBase: FBtp0064874
S. cerevisiae: Strain background: W303	ATCC	ATTC: 208353
Mouse: R6/2: B6CBA-Tg(HDexon1)62Gpb/3J	The Jackson Laboratory	JAX: 006494
Mouse: OXTRfl/fl: B6.129(SJL)-$Oxtr^{tm1.1Wsy}$/J	The Jackson Laboratory	RRID: IMSR_JAX:008471
Zebrafish: Tg(Shha:GFP)t10: t10Tg	Neumann and Nuesslein-Volhard, 2000	ZFIN: ZDB-GENO-060207-1
Arabidopsis: 35S::PIF4-YFP, BZR1-CFP	Wang et al., 2012	N/A
Arabidopsis: JYB1021.2: pS24(AT5G58010)::cS24:GFP(-G):NOS #1	NASC	NASC ID: N70450
Recombinant DNA		
pLVX-Tight-Puro (TetOn)	Clonetech	Cat#632162
Plasmid: GFP-Nito	This paper	N/A

REAGENT or RESOURCE	SOURCE	IDENTIFIER
cDNA GH111110	Drosophila Genomics Resource Center	DGRC:5666; FlyBase:FBcl0130415
AAV2/1-hsyn-GCaMP6-WPRE	Chen et al., 2013	N/A
Mouse raptor: pLKO mouse shRNA 1 raptor	Thoreen et al., 2009	Addgene Plasmid #21339
Sequence-Based Reagents		
siRNA targeting sequence: PIP5K I alpha #1: ACACAGUACUCAGUUGAUA	This paper	N/A
Primers for XX, see Table SX	This paper	N/A
Primer: GFP/YFP/CFP Forward: GCACGACTTCTTCAAGTCCGCCATGCC	This paper	N/A
Morpholino: MO-pax2a GGTCTGCTTTGCAGTGAATATCCAT	Gene Tools	ZFIN: ZDB-MRPHLNO-061106-5
ACTB (hs01060665_g1)	Life Technologies	Cat#4331182
RNA sequence: hnRNPA1_ligand: UAGGGACUUAGGGUUCUCUCUAGGGACUUAGGGUUCUCUCUAGGGA	This paper	N/A
Software and Algorithms		
Bowtie2	Langmead and Salzberg, 2012	http://bowtie-bio.sourceforge.net/bowtie2/index.shtml
Samtools	Li et al., 2009	http://samtools.sourceforge.net/
Other		
Sequence data, analyses, and resources related to the ultra-deep sequencing of the AML31 tumor, relapse, and matched normal.	This paper	http://aml31.genome.wustl.edu
Resource website for the AML31 publication	This paper	https://github.com/chrisamiller/aml31SuppSite

CONTACT FOR REAGENT AND RESOURCE SHARING

Further information and requests for resources and reagents should be directed to and will be fulfilled by the Lead Contact Guo-li Ming (gming@pennmedicine.upenn.edu). There are no restrictions on any data or materials presented in this paper.

EXPERIMENTAL MODEL AND SUBJECT DETAILS

Animals—All animal procedures used in this study were performed in accordance with the protocol approved by the Institutional Animal Care and Use Committee of Johns Hopkins University School of Medicine, University of Pennsylvania School of Medicine, and The Hong Kong University of Science and Technology. Six mouse lines were used for this study: C57Bl6/J mice, *Pirt-GCaMP3* mice (Kim et al., 2016), *Mettl14*$^{f/f}$ mice (Yoon et al., 2017); *Syn1-Cre* mice (JAX 003966), *Ythdf1*$^{-/-}$ mice (manuscript in preparation), and *Pten*$^{f/f}$ mice (Bonaguidi et al., 2011). Adult mice (6-8 weeks) were used. Housing and husbandry conditions followed standard settings. Experimental and control mice were male littermates housed together before the experiment.

METHOD DETAILS

AAV constructs—The recombinant AAV2/9 vectors for Cre and GFP were from the UPenn Vector Core. AAV2 for shRNA-control and shRNA-Mettl14 were constructed and prepared in house.

Animal surgery—Intrathecal injection of AAV2/9 was performed in adult 6-8 weeks old male mice as previously described (Weng et al., 2017). Briefly, 3 μl of viral solution was injected into the cerebrospinal fluid between vertebrae L5 and L6 using a 30 gauge Hamilton syringe slowly over 2 min followed an additional 2-minute wait to allow the fluid to diffuse.

Following the injection, the mice were left undisturbed for 3 weeks for recovery and for complete dissemination of the virus.

For sciatic nerve lesion (SNL), mice were anesthetized and a small incision was made on the skin at the mid-thigh level. The sciatic nerve was exposed after opening the fascial plane between the gluteus superficialis and biceps femoris muscles. The nerve was carefully freed from surrounding connective tissue and then crushed for 15 s at 3 clicks of ultra-fine hemostatic forceps (F.S.T. 13021-12). The crush site was labeled by Fluoro-Max dyed blue aqueous fluorescent particles (ThermoFisher; B0100; Figure S4D). Skin was then closed with two suture clips. For the sham surgery (the naïve conditions), the sciatic nerve in the contralateral side was exposed and mobilized but left uninjured. For the thermal withdrawal test and skin biopsy experiments, the saphenous nerve was ligated and transected above the knee region after sciatic nerve crush, so that the hindpaw epidermis could only be innervated by regenerating sciatic nerve axons.

For optic nerve injury, the procedure was performed as previously described (Park et al., 2008). Briefly, individual AAV-shRNA-control or AAV-shRNA-Mettl14 was mixed with AAV-Cre and intravitreally injected to the left eye of adult WT or *Pten*$^{f/f}$ mice. Two weeks after viral injection, the left optic nerve was exposed intraorbitally and crushed with jeweler's forceps (Dumont number 5; Roboz) for 5 s, approximately 1 mm behind the optic disc. To visualize regenerating axons, RGC axons in the optic nerve were anterogradely labeled by 1 μl of cholera toxin β subunit (CTB; 2 μg/μl; Invitrogen) 12 days after injury. Animals were fixed by 4% PFA 2 days after CTB injection in the eye. Quantification of regenerating axons was also performed according the previously described method (Park et al., 2008).

DRG cultures and neurite outgrowth assay—DRG primary culture was performed as previously described (Chen et al., 2016). Briefly, mice were anesthetized and perfused with sterile PBS. L4-L6 DRGs were dissected, washed in cold HBSS medium and then digested in 0.1% collagenase (Invitrogen; 17100017) in HBSS for 90 min. After triturated into single cell suspension, DRG neurons were precipitated at room temperature for 20 min and plated on a coated culture dish. Cultures were infected with AAV co-expressing Cre and different shRNAs (See KEY RESOURCE TABLE). For re-plating, DRG neurons cultured with AAV for 10 days were gently flushed, resuspended and replated on a coated culture dish. The replated neurons were cultured for another one day and fixed for Tuj1 staining. The average lengths of longest neurites from each DRG neurons were measured and quantified by ImageJ.

m^{6}A-SMART-seq—mRNA from total RNA of adult mouse DRGs was purified with Dynabeads Oligo $(dT)_{25}$ (ThermoFisher; 61006). Five μg of anti-m^{6}A polyclonal antibody (Synaptic Systems; 202003) was conjugated to Dynabeads Protein A (ThermoFisher; 10001D) overnight at 4°C. A total of 150 ng of mRNA was then incubated with the antibody/beads in 1× IP buffer (10 mM Tris-HCL, 150 mM NaCl, and 0.1% (vol/vol) Igepal CA-630), supplemented with 200 U SUPERase In RNase Inhibitor (ThermoFisher; AM2696), for 2 hr at 4°C. After incu bation, the beads were washed 3 times with IP buffer and the m^{6}A RNA was eluted twice with 6.7 mM N^6-Methyladenosine (Sigma-Aldrich;

M2780) in 1× IP buffer. The eluted RNA was extracted with Trizol reagent (ThermoFisher; 15596018) and recovered by RNA Clean and Concentrator-5 spin columns (Zymo; R1015). The equivalent amount of input and m^{6}A-IPed RNA were prepared for library generation using the SMART-seq protocol as described (Picelli et al., 2014). Two biological replicates of naïve and SNL conditions were sequenced using Illumina NextSeq 500.

m^{6}A-CLIP-SMART-seq—A total of 150 ng mRNA was first fragmented to ~ 100 nt by RNA Fragmentation Reagent (ThermoFisher; AM8740) at 70°C for 8 min. After the reaction was stopped by 100 mM EDTA, the RNA mixtures were then directly diluted to 450 μl CLIP buffer (150 mM NaCl, 0.1% NP-40, 10 mM Tris-HCl (pH 7.4)) with 5 g anti-m^{6}A polyclonal antibody (Synaptic Systems; 202003) and incubated at 4 °C for 2 hr. Anti-m^{6}A antibody - RNA interactions were stabilized with UV crosslinking (254 nm, 150 mJ/cm^2) twice in a Stratalinker (Agilent). Antibody-RNA complexes were then precipitated with 50 l Protein A/G beads (Thermo Scientific) for 2 hr at 4 °C, followed by two stringent washes (50 mM Tris, pH 7.4, 1 M NaCl, 1 mM EDTA, 1% NP-40, 0.1% SDS) and two CLIP buffer washes. After dephosphorylation with 10 U FastAP (ThermoFisher; EF0652) at 10 min at room temperature and polyadenylation with 5U E. coli Poly(A) Polymerase (NEB, M0276S) for 15 min at room temperature on beads, the RNA was then eluted by treatment with proteinase K (Thermo Scientific; 25530049) at 37°C for 1 hr. The eluted RNA was extracted with Trizol reagent (ThermoFisher; 15596018) and recovered by RNA Clean and Concentrator-5 spin columns (Zymo; R1015). The m^{6}A CLIP library was prepared using a modified SMART-seq2 protocol without tagmentation. Briefly, RNA was first primed with customized dT primer (GTCTCGTGGGCTCGGAGATGTGTATAAGAGACAG T_{30}VN) and incubated with RT master mix containing customized TSO primer (TCGTCGGCAGCGTCAGATGTGTATAAGAGACArGrGrG) at 42°C for 1.5 hr. Libraries were PCR amplified for 1 9 cycles, size selected via BluePippin and sequenced on Illumina NextSeq 500.

RNA-seq—Total RNA of L4/L5 DRGs was isolated from WT and Syn1-Cre;*Mettl14*$^{f/f}$ cKO mice, extracted with Trizol reagent (ThermoFisher; 15596018) and recovered by RNA Clean and Concentrator-5 spin columns (Zymo; R1015). The RNAseq library was prepared using the Smart-seq2 protocol. The distribution of fragment sizes was verified. Libraries of three biological replicates under different conditions were uniquely barcoded, pooled at equimolar concentrations, and sequenced on Illumina NextSeq 500 (Su et al., 2017).

Analysis m^{6}A-SMART-Seq and RNA-seq—Adapters were trimmed from original reads using Trimmomatic and low-quality reads were removed. The remaining reads were then mapped to the mouse genome (mm10) using STAR aligner (Dobin et al., 2013). To measure the relative m^{6}A level per gene, the ratio of m^{6}A IP/ Input was first calculated. The Z scores were then obtained by comparing the ratios (m^{6}A IP/ Input) to the mean of the group to reflect the relative m^{6}A level per gene on a transcriptome-wide scale (Batista et al., 2014). GAPDH is barely methylated (validated by m^{6}A-MeRIP Q-PCR) with Z score < 0. We set Z score > 0 as a threshold to obtain genes with modest to high m^{6}A levels. Shared m^{6}A-tagged genes in two biological replicates were identified as high confidence m^{6}A-tagged transcripts for downstream analysis. The gene list of RAGs was obtained from the

magenta module in the previous study (Chandran et al., 2016). For the comparison of m^{6}A transcriptomes between naïve and SNL D1 conditions, m^{6}A-tagged transcript levels were presented as mean TPM (Mean transcripts per kilobase million). The top 400 differentially m^{6}A-tagged genes were uploaded to the Panther Classification System for a statistical overrepresentation test.

Analysis of m^{6}A-CLIP-SMART-seq—Adapters, and the first three nucleotides of the sequencing read (derived from the TSO oligo) were removed by Trimmomatic. The remaining reads (> 20 nt) were then mapped to the mouse genome (mm10) using STAR aligner (–outFilterMultimapNmax 1 –outFilterMismatchNoverLmax 0.08 –alignEndsType EndToEnd). After removal of PCR duplicates, uniquely mapped reads were used for CIMS analysis similar to previous studies (Linder et al., 2015; Moore et al., 2014; Zhang and Darnell, 2011). All mutations were considered as signals. The number of overlapping unique tags (*k*) and the number of tags with mutations (*m*) at the position were determined using the CIMS algorithm. The m/k was restricted to between 1% and 50% to reduce noise and remove SNP and mis-mapping artifacts. Only m^{6}A residues in DRACH consensus sequence were considered for the downstream analysis. The list of genes with differential m^{6}A-tag numbers (gain > 3 or lost > 2) was uploaded to the Panther Classification System for a statistical overrepresentation test.

m^{6}A-MeRIP Q-PCR—The m^{6}A-modified control spike-in RNA (eGFP, 0.7 kb) was synthesized by in vitro transcription using the mMessage mMachine T7 Ultra kit (ThermoFisher; AM1345). A total of 150 ng of input mRNA was mixed with 10 pg of control spike-in RNA and subjected to m^{6}A-IP as described above. Immunoprecipitated RNA was purified and reverse-transcribed with Oligo (dT) primer using SMARTScribe Reverse Transcriptase (Clontech; 639537). Indicated genes were analyzed by Q-PCR using Fast SYBR Green Master Mix (ThermoFisher; 4385612) and normalized to the spike-in eGFP RNA levels. Relative fold change was calculated as the ratio of normalized transcript levels between naïve and SNL D1 conditions. Primer sequences are listed in Table S3.

m^{6}A dot blot analysis—mRNA was harvested from homogenized WT and *Mettl14* cKO DRGs using Dynabeads mRNA Direct Purification Kit (Ambion; 61011). Three biological replicates were pooled for each sample to ensure sufficient concentration of mRNA. Duplicates of 100 ng mRNA per 1 μl were applied to an Amersham Hybond-N$^+$ membrane (GE Healthcare) as previously described (Yoon et al., 2017). UV crosslinking of RNA to the membrane was performed by running the auto-crosslink program twice in Stratalinker 2400. The membrane was then washed in PBST three times and blocked with 5% skim milk in PBST for 2 hr. After an additional PBST wash, primary anti-m^{6}A antibody (Synaptic Systems; 212B11) at 1:1000 dilution was applied for 2 hr incubation at room temperature. After 3 washes in PBST, the membrane was incubated in HRP-conjugated anti-mouse IgG secondary antibody for 2 hr at room temperature, then washed again 3 times in PBST. Finally, the signal was visualized using SuperSignal West Dura Extended Duration Substrate (Thermo Scientific; 34075). To confirm equal mRNA loading, the same membrane was stained with 0.02% methylene blue in 0.3 M sodium acetate (pH 5.2). Quantified m^{6}A levels were normalized to the amount of mRNA loaded.

Immunohistology, imaging and analysis—Immunohistology was performed as described previously (Weng et al., 2017). Briefly, samples were collected from perfused animals, post-fixed overnight in 4% PFA in PBS, and cryoprotected in 30% sucrose (wt/vol) for 24 hr at 4°C. Samples were sec tioned to 20 m and mounted onto slides. Primary antibody was applied at 4°C overnight. Seco ndary antibody was applied for 2 hr at room temperature. The following primary antibodies were used in this study: rabbit anti-m6A (Synaptic Systems; 212B11; 1:2000), rabbit anti-ATF3 (Santa Cruz; sc-188; 1:500), rabbit anti-PGP9.5 (AbD Serotec; 7863-0504; 1:800), rabbit anti-SCG10 (Novus Biologicals; NBP1-49461, 1: 2000), and anti-cleaved (active) form of caspase 3 (Invitrogen; 9H19L2; 1:500). Secondary antibodies corresponding to the primary antibody species were Cy2–, Cy3– or Cy5 conjugated (Jackson ImmunoResearch; 1:500). The images were acquired by confocal microscopy (Zeiss 710) and analyzed with ImageJ software (National Institutes of Health).

Quantification of the proportion of $ATF3^+$ neurons was determined by counting and scoring at least 200 neurons/mouse as $ATF3^+$ or $ATF3^-$ (Weng et al., 2017). A cell was scored as $ATF3^+$ if there was any fluorescence above the threshold set in $ATF3^-$ cells under the naïve conditions. Sections were randomly chosen from cross-sectioned L4/L5 DRGs.

Measurement of newly synthesized protein—WT and *Syn1-Cre;Mettl14*$^{f/f}$ (cKO) mice at 8-10 weeks of age were injected with puromycin (10 mg/kg, intraperitoneal, i.p.) at SNL D1. After 1 hr labeling, L4/L5 naïve or injured DRGs were collected and processed for Western blot as previously described (Weng et al., 2017). Briefly, protein samples were separated by 10% Mini-PROTEAN TGX™ Precast Protein Gels (Bio-rad) and transferred to PVDF membrane using the transblot turbo system (Biorad) following manufacturer's instructions. The membrane was incubated in blocking buffer (5% non-fat dry milk and 0.1% Tween 20 in TBS) for 1 hr at room temperature and then in mouse anti-puromycin antibody (MABE343; Millipore; 1:1000) at 4°C overnight. The blots were washed and incubated in HRP-conjugated goat anti-mouse IgG (Santa Cruz; sc-2031; 1:5000) at room temperature for 1 hr. Membranes were stripped and re-blotted with rabbit anti-GAPDH antibodies (Abcam; ab9485; 1:2000) as the loading control. Newly synthesized protein was quantified by measuring signal intensities at different size ranges from 198 to 15 KDa. Signals were quantified using ImageJ and data were normalized to that of the WT naïve conditions in the same blots.

Capillary electrophoresis immunoassay—The time course of the expression of ATF3 protein was determined by the capillary electrophoresis immunoassay using the Simple Western system as described previously. In brief, L4/L5 naïve or injured DRGs were collected 1, 3, and 7 days post-SNL. Tissues were homogenized in CelLytic M (Sigma; C2978) containing a protease inhibitor cocktail (Sigma; 4693159001). The lysate protein concentration was determined using the Pierce BCA protein assay kit (Thermo Scientific; 23227). Equal amounts of DRG lysates (1 μg) were mixed with Simple Western reagents and loaded to each capillary. The primary antibodies were diluted with antibody diluent (ProteinSimple) at 1:50 for ant-ATF3 (Santa Cruz; sc-188), 1:50 for anti-Mettl14 (Proteintech; 26158-1-AP), and 1:50 for anti-GAPDH (Abcam; ab9485).

Western blot analysis—L4/L5 injured or naive DRGs were rapidly dissected and extracted protein samples were run on 10% Mini-PROTEAN TGX Precast Protein Gels (Bio-rad) and transferred to PVDF membrane. The membrane was blocked overnight in 5% dry milk at 4°C with rocking. Rabbit anti-YTHDF1 antibody (Proteintech; 1:1000) was applied overnight at 4°C followed by HRP-conjugated anti-rabbit IgG antibody (Santa Cruz; 1:10000). Protein loading was verified by mouse anti-GAPDH (EMD Millipore; AB2302).

In vivo DRG axon regeneration assay—To measure regeneration of the sciatic nerve, samples were collected at SNL D3 and prepared as described above. Samples were sectioned longitudinally at 30 m and stained with SCG10 (Novus Biologicals, NBP1-49461). An SCG10 intensity plot was created using average intensities calculated across 10 μm non-overlapping regions and normalized. Intensity was measured by Image J as previously described (Di Maio et al., 2011; Shin et al., 2012; Weng et al., 2017)

Punch biopsies of glabrous footpad skin from hind paws were collected for the quantification of nerve re-innervation (see Figure S2J in (Weng et al., 2017)). The biopsy was prepared and post-fixed in Zamboni's fixative. Samples were mounted on gelatin-coated slides and stained with rabbit anti-PGP9.5 which visualizes nerve fibers. To quantify regeneration, nerve fiber density was counted across 3 zones (defined in Figure 2F in (Weng et al., 2017)).

Behavioral analysis—The thermal withdrawal behavioral test was performed following a previously established protocol (Wright et al., 2014). Briefly, the mice were placed on a glass surface with a consistent temperature of 30°C. The plantar surface of the hindpaw was hea ted using a focused, radiant heat light source (model 33 Analgesia Meter; IITC/Life Science Instruments, Woodland Hills, CA, USA). A timer linked to the light source was used to measure the paw-withdrawal latency. Only quick hind paw movements away from the stimulus were considered to be a withdrawal response, and seven individual measurements were repeated for each paw (Weng et al., 2017).

Optic nerve regeneration quantifications—Quantification was performed as previously described (Park et al., 2008). For RGC regenerating axon quantification, the number of axons at different distances from the injury site was estimated by the following formula: $\Sigma ad=\pi r^2\times$ [average axon numbers per mm/t], where r is equal to half the width of the nerve at the counting site, the average number of axons per millimeter is equal to the average of (axon number)/(nerve width) in four sections of one optic nerve, and t is equal to the section thickness (8 μm). For RGC survival and $pS6^+$ RGCs quantification in the whole mount retina preparation, twelve images (three from each quarter, covering from inner to outer retina) of each retina were captured under a confocal microscope. $Tuj1^+$ or $pS6^+$ RGCs were quantified in a blinded fashion. Quantification of $SMI32^+$ RGCs was performed from images of Tuj1 and SMI32 immunostaining on retina sections.

QUANTIFICATION AND STATISTICAL ANALYSIS

Data in figure panels reflect several independent experiments performed on different days.

The number of animals used for experiments is listed in the figure legends. An estimate of variation within each group of data is indicated using standard error of the mean (SEM). We performed two-way ANOVA tests for assessing the significance of differences between two treatments based the data properties or as indicated in the figure legends.

DATA AND SOFTWARE AVAILABILITY

The access number for the data for m^{6}A-SMART-seq, m^{6}A-SMART-CLIP-seq, and RNA-seq reported in this study is NCBI GEO: GSE106423.

Supplementary Material

Refer to Web version on PubMed Central for supplementary material.

Acknowledgments

We thank members of Ming and Song laboratories, and The Dr. Miriam and Sheldon G. Adelson Medical Research Foundation (AMRF) investigators for discussion, J. Schnoll and K. Christian for comments, and Y. Cai, L. Liu, and D. Johnson for technical support. This work was supported by grants from AMRF (to G-l.M.), National Institutes of Health (P01NS097206 and RM1HG008935 to H.S., J.P., and C.H., R37NS047344 to H.S., and R35NS097370 to G-l.M.), Hong Kong Research Grants Council (16103315 and 16149316 to K.L.), and National Natural Science Foundation of China (81671214 to K.L.). C.H. is an HHMI investigator.

References

Abe N, Borson SH, Gambello MJ, Wang F, Cavalli V. Mammalian target of rapamycin (mTOR) activation increases axonal growth capacity of injured peripheral nerves. J Biol Chem. 2010; 285:28034–28043. [PubMed: 20615870]

Batista PJ, Molinie B, Wang J, Qu K, Zhang J, Li L, Bouley DM, Lujan E, Haddad B, Daneshvar K, et al. m(6)A RNA modification controls cell fate transition in mammalian embryonic stem cells. Cell Stem Cell. 2014; 15:707–719. [PubMed: 25456834]

Befort K, Karchewski L, Lanoue C, Woolf CJ. Selective up-regulation of the growth arrest DNA damage-inducible gene Gadd45 alpha in sensory and motor neurons after peripheral nerve injury. The European journal of neuroscience. 2003; 18:911–922. [PubMed: 12925017]

Belin S, Nawabi H, Wang C, Tang S, Latremoliere A, Warren P, Schorle H, Uncu C, Woolf CJ, He Z, et al. Injury-induced decline of intrinsic regenerative ability revealed by quantitative proteomics. Neuron. 2015; 86:1000–1014. [PubMed: 25937169]

Bonaguidi MA, Wheeler MA, Shapiro JS, Stadel RP, Sun GJ, Ming GL, Song H. In vivo clonal analysis reveals self-renewing and multipotent adult neural stem cell characteristics. Cell. 2011; 145:1142–1155. [PubMed: 21664664]

Chandran V, Coppola G, Nawabi H, Omura T, Versano R, Huebner EA, Zhang A, Costigan M, Yekkirala A, Barrett L, et al. A Systems-Level Analysis of the Peripheral Nerve Intrinsic Axonal Growth Program. Neuron. 2016; 89:956–970. [PubMed: 26898779]

Chen W, Lu N, Ding Y, Wang Y, Chan LT, Wang X, Gao X, Jiang S, Liu K. Rapamycin-Resistant mTOR Activity Is Required for Sensory Axon Regeneration Induced by a Conditioning Lesion. eNeuro. 2016; 3

Cho Y, Cavalli V. HDAC signaling in neuronal development and axon regeneration. Curr Opin Neurobiol. 2014; 27:118–126. [PubMed: 24727244]

Cho Y, Park D, Cavalli V. Filamin A is required in injured axons for HDAC5 activity and axon regeneration. J Biol Chem. 2015; 290:22759–22770. [PubMed: 26157139]

Cho Y, Sloutsky R, Naegle KM, Cavalli V. Injury-induced HDAC5 nuclear export is essential for axon regeneration. Cell. 2013; 155:894–908. [PubMed: 24209626]

Costigan M, Befort K, Karchewski L, Griffin RS, D'Urso D, Allchorne A, Sitarski J, Mannion JW, Pratt RE, Woolf CJ. Replicate high-density rat genome oligonucleotide microarrays reveal

hundreds of regulated genes in the dorsal root ganglion after peripheral nerve injury. BMC Neurosci. 2002; 3:16. [PubMed: 12401135]

Cui Q, Shi H, Ye P, Li L, Qu Q, Sun G, Sun G, Lu Z, Huang Y, Yang CG, et al. m6A RNA Methylation Regulates the Self-Renewal and Tumorigenesis of Glioblastoma Stem Cells. Cell Rep. 2017; 18:2622–2634. [PubMed: 28297667]

Desrosiers RC, Friderici KH, Rottman FM. Characterization of Novikoff hepatoma mRNA methylation and heterogeneity in the methylated 5′ terminus. Biochemistry. 1975; 14:4367–4374. [PubMed: 169893]

Di Maio A, Skuba A, Himes BT, Bhagat SL, Hyun JK, Tessler A, Bishop D, Son YJ. In vivo imaging of dorsal root regeneration: rapid immobilization and presynaptic differentiation at the CNS/PNS border. J Neurosci. 2011; 31:4569–4582. [PubMed: 21430157]

Dobin A, Davis CA, Schlesinger F, Drenkow J, Zaleski C, Jha S, Batut P, Chaisson M, Gingeras TR. STAR: ultrafast universal RNA-seq aligner. Bioinformatics. 2013; 29:15–21. [PubMed: 23104886]

Dominissini D, Moshitch-Moshkovitz S, Schwartz S, Salmon-Divon M, Ungar L, Osenberg S, Cesarkas K, Jacob-Hirsch J, Amariglio N, Kupiec M, et al. Topology of the human and mouse m6A RNA methylomes revealed by m6A-seq. Nature. 2012; 485:201–206. [PubMed: 22575960]

Donnelly CJ, Park M, Spillane M, Yoo S, Pacheco A, Gomes C, Vuppalanchi D, McDonald M, Kim HH, Merianda TT, et al. Axonally synthesized beta-actin and GAP-43 proteins support distinct modes of axonal growth. J Neurosci. 2013; 33:3311–3322. [PubMed: 23426659]

Duan X, Qiao M, Bei F, Kim IJ, He Z, Sanes JR. Subtype-specific regeneration of retinal ganglion cells following axotomy: effects of osteopontin and mTOR signaling. Neuron. 2015; 85:1244–1256. [PubMed: 25754821]

Fagoe ND, Attwell CL, Kouwenhoven D, Verhaagen J, Mason MR. Overexpression of ATF3 or the combination of ATF3, c-Jun, STAT3 and Smad1 promotes regeneration of the central axon branch of sensory neurons but without synergistic effects. Human molecular genetics. 2015; 24:6788–6800. [PubMed: 26385639]

Finelli MJ, Wong JK, Zou H. Epigenetic regulation of sensory axon regeneration after spinal cord injury. J Neurosci. 2013; 33:19664–19676. [PubMed: 24336730]

Gaub P, Joshi Y, Wuttke A, Naumann U, Schnichels S, Heiduschka P, Di Giovanni S. The histone acetyltransferase p300 promotes intrinsic axonal regeneration. Brain. 2011; 134:2134–2148. [PubMed: 21705428]

Geula S, Moshitch-Moshkovitz S, Dominissini D, Mansour AA, Kol N, Salmon-Divon M, Hershkovitz V, Peer E, Mor N, Manor YS, et al. Stem cells. m6A mRNA methylation facilitates resolution of naive pluripotency toward differentiation. Science. 2015; 347:1002–1006. [PubMed: 25569111]

Gilbert WV, Bell TA, Schaening C. Messenger RNA modifications: Form, distribution, and function. Science. 2016; 352:1408–1412. [PubMed: 27313037]

Goodman CA, Mabrey DM, Frey JW, Miu MH, Schmidt EK, Pierre P, Hornberger TA. Novel insights into the regulation of skeletal muscle protein synthesis as revealed by a new nonradioactive in vivo technique. FASEB journal : official publication of the Federation of American Societies for Experimental Biology. 2011; 25:1028–1039. [PubMed: 21148113]

Guo JU, Su Y, Zhong C, Ming GL, Song H. Emerging roles of TET proteins and 5-hydroxymethylcytosines in active DNA demethylation and beyond. Cell cycle. 2011; 10:2662–2668. [PubMed: 21811096]

Haussmann IU, Bodi Z, Sanchez-Moran E, Mongan NP, Archer N, Fray RG, Soller M. m6A potentiates Sxl alternative pre-mRNA splicing for robust Drosophila sex determination. Nature. 2016; 540:301–304. [PubMed: 27919081]

Jankowski MP, McIlwrath SL, Jing X, Cornuet PK, Salerno KM, Koerber HR, Albers KM. Sox11 transcription factor modulates peripheral nerve regeneration in adult mice. Brain Res. 2009; 1256:43–54. [PubMed: 19133245]

Jia G, Fu Y, Zhao X, Dai Q, Zheng G, Yang Y, Yi C, Lindahl T, Pan T, Yang YG, et al. N6-methyladenosine in nuclear RNA is a major substrate of the obesity-associated FTO. Nat Chem Biol. 2011; 7:885–887. [PubMed: 22002720]

Jung H, Yoon BC, Holt CE. Axonal mRNA localization and local protein synthesis in nervous system assembly, maintenance and repair. Nat Rev Neurosci. 2012; 13:308–324. [PubMed: 22498899]

Ke S, Alemu EA, Mertens C, Gantman EC, Fak JJ, Mele A, Haripal B, Zucker-Scharff I, Moore MJ, Park CY, et al. A majority of m6A residues are in the last exons, allowing the potential for 3′ UTR regulation. Genes Dev. 2015; 29:2037–2053. [PubMed: 26404942]

Kim YS, Anderson M, Park K, Zheng Q, Agarwal A, Gong C, Saijilafu, Young L, He S, LaVinka PC, et al. Coupled Activation of Primary Sensory Neurons Contributes to Chronic Pain. Neuron. 2016; 91:1085–1096. [PubMed: 27568517]

Lence T, Akhtar J, Bayer M, Schmid K, Spindler L, Ho CH, Kreim N, Andrade-Navarro MA, Poeck B, Helm M, et al. m6A modulates neuronal functions and sex determination in Drosophila. Nature. 2016; 540:242–247. [PubMed: 27919077]

Li A, Chen YS, Ping XL, Yang X, Xiao W, Yang Y, Sun HY, Zhu Q, Baidya P, Wang X, et al. Cytoplasmic m6A reader YTHDF3 promotes mRNA translation. Cell research. 2017a; 27:444–447. [PubMed: 28106076]

Li HB, Tong J, Zhu S, Batista PJ, Duffy EE, Zhao J, Bailis W, Cao G, Kroehling L, Chen Y, et al. m6A mRNA methylation controls T cell homeostasis by targeting the IL-7/STAT5/SOCS pathways. Nature. 2017b; 548:338–342. [PubMed: 28792938]

Li L, Zang L, Zhang F, Chen J, Shen H, Shu L, Liang F, Feng C, Chen D, Tao H, et al. Fat mass and obesity-associated (FTO) protein regulates adult neurogenesis. Human molecular genetics. 2017c

Li X, Xiong X, Yi C. Epitranscriptome sequencing technologies: decoding RNA modifications. Nat Methods. 2016; 14:23–31. [PubMed: 28032622]

Lin S, Choe J, Du P, Triboulet R, Gregory RI. The m(6)A Methyltransferase METTL3 Promotes Translation in Human Cancer Cells. Mol Cell. 2016; 62:335–345. [PubMed: 27117702]

Linder B, Grozhik AV, Olarerin-George AO, Meydan C, Mason CE, Jaffrey SR. Single-nucleotide-resolution mapping of m6A and m6Am throughout the transcriptome. Nat Methods. 2015; 12:767–772. [PubMed: 26121403]

Liu K, Lu Y, Lee JK, Samara R, Willenberg R, Sears-Kraxberger I, Tedeschi A, Park KK, Jin D, Cai B, et al. PTEN deletion enhances the regenerative ability of adult corticospinal neurons. Nat Neurosci. 2010; 13:1075–1081. [PubMed: 20694004]

Liu K, Tedeschi A, Park KK, He Z. Neuronal intrinsic mechanisms of axon regeneration. Annual review of neuroscience. 2011; 34:131–152.

Meyer KD, Patil DP, Zhou J, Zinoviev A, Skabkin MA, Elemento O, Pestova TV, Qian SB, Jaffrey SR. 5′ UTR m(6)A Promotes Cap-Independent Translation. Cell. 2015; 163:999–1010. [PubMed: 26593424]

Meyer KD, Saletore Y, Zumbo P, Elemento O, Mason CE, Jaffrey SR. Comprehensive analysis of mRNA methylation reveals enrichment in 3′ UTRs and near stop codons. Cell. 2012; 149:1635–1646. [PubMed: 22608085]

Molinie B, Wang J, Lim KS, Hillebrand R, Lu ZX, Van Wittenberghe N, Howard BD, Daneshvar K, Mullen AC, Dedon P, et al. m(6)A-LAIC-seq reveals the census and complexity of the m(6)A epitranscriptome. Nat Methods. 2016; 13:692–698. [PubMed: 27376769]

Moore DL, Goldberg JL. Multiple transcription factor families regulate axon growth and regeneration. Developmental neurobiology. 2011; 71:1186–1211. [PubMed: 21674813]

Moore MJ, Zhang C, Gantman EC, Mele A, Darnell JC, Darnell RB. Mapping Argonaute and conventional RNA-binding protein interactions with RNA at single-nucleotide resolution using HITS-CLIP and CIMS analysis. Nature protocols. 2014; 9:263–293. [PubMed: 24407355]

Park KK, Liu K, Hu Y, Smith PD, Wang C, Cai B, Xu B, Connolly L, Kramvis I, Sahin M, et al. Promoting axon regeneration in the adult CNS by modulation of the PTEN/mTOR pathway. Science. 2008; 322:963–966. [PubMed: 18988856]

Perlson E, Hanz S, Ben-Yaakov K, Segal-Ruder Y, Seger R, Fainzilber M. Vimentin-dependent spatial translocation of an activated MAP kinase in injured nerve. Neuron. 2005; 45:715–726. [PubMed: 15748847]

Picelli S, Faridani OR, Bjorklund AK, Winberg G, Sagasser S, Sandberg R. Full-length RNA-seq from single cells using Smart-seq2. Nature protocols. 2014; 9:171–181. [PubMed: 24385147]

Puttagunta R, Tedeschi A, Soria MG, Hervera A, Lindner R, Rathore KI, Gaub P, Joshi Y, Nguyen T, Schmandke A, et al. PCAF-dependent epigenetic changes promote axonal regeneration in the central nervous system. Nature communications. 2014; 5:3527.

Rishal I, Fainzilber M. Axon-soma communication in neuronal injury. Nat Rev Neurosci. 2014; 15:32–42. [PubMed: 24326686]

Schmidt EK, Clavarino G, Ceppi M, Pierre P. SUnSET, a nonradioactive method to monitor protein synthesis. Nature methods. 2009; 6:275–277. [PubMed: 19305406]

Seijffers R, Mills CD, Woolf CJ. ATF3 increases the intrinsic growth state of DRG neurons to enhance peripheral nerve regeneration. J Neurosci. 2007; 27:7911–7920. [PubMed: 17652582]

Shi H, Wang X, Lu Z, Zhao BS, Ma H, Hsu PJ, Liu C, He C. YTHDF3 facilitates translation and decay of N6-methyladenosine-modified RNA. Cell research. 2017; 27:315–328. [PubMed: 28106072]

Shin JE, Cho Y, Beirowski B, Milbrandt J, Cavalli V, DiAntonio A. Dual leucine zipper kinase is required for retrograde injury signaling and axonal regeneration. Neuron. 2012; 74:1015–1022. [PubMed: 22726832]

Shin JE, Geisler S, DiAntonio A. Dynamic regulation of SCG10 in regenerating axons after injury. Exp Neurol. 2014; 252:1–11. [PubMed: 24246279]

Smith DS, Skene JH. A transcription-dependent switch controls competence of adult neurons for distinct modes of axon growth. J Neurosci. 1997; 17:646–658. [PubMed: 8987787]

Song H, Poo M. The cell biology of neuronal navigation. Nature cell biology. 2001; 3:E81–88. [PubMed: 11231595]

Su Y, Shin J, Zhong C, Wang S, Roychowdhury P, Lim J, Kim D, Ming GL, Song H. Neuronal activity modifies the chromatin accessibility landscape in the adult brain. Nat Neurosci. 2017; 20:476–483. [PubMed: 28166220]

Tedeschi A, Bradke F. Spatial and temporal arrangement of neuronal intrinsic and extrinsic mechanisms controlling axon regeneration. Curr Opin Neurobiol. 2016; 42:118–127. [PubMed: 28039763]

Trakhtenberg EF, Goldberg JL. Epigenetic regulation of axon and dendrite growth. Front Mol Neurosci. 2012; 5:24. [PubMed: 22403528]

van Niekerk EA, Tuszynski MH, Lu P, Dulin JN. Molecular and Cellular Mechanisms of Axonal Regeneration After Spinal Cord Injury. Mol Cell Proteomics. 2016; 15:394–408. [PubMed: 26695766]

Walters BJ, Mercaldo V, Gillon CJ, Yip M, Neve RL, Boyce FM, Frankland PW, Josselyn SA. The Role of The RNA Demethylase FTO (Fat Mass and Obesity-Associated) and mRNA Methylation in Hippocampal Memory Formation. Neuropsychopharmacology. 2017; 42:1502–1510. [PubMed: 28205605]

Wang X, Huang J, Zou T, Yin P. Human m6A writers: Two subunits, two roles. RNA Biol. 2017; 14:300–304. [PubMed: 28121234]

Wang X, Zhao BS, Roundtree IA, Lu Z, Han D, Ma H, Weng X, Chen K, Shi H, He C. N(6)-methyladenosine Modulates Messenger RNA Translation Efficiency. Cell. 2015; 161:1388–1399. [PubMed: 26046440]

Wang Y, Li Y, Toth JI, Petroski MD, Zhang Z, Zhao JC. N6-methyladenosine modification destabilizes developmental regulators in embryonic stem cells. Nature cell biology. 2014; 16:191–198. [PubMed: 24394384]

Weng YL, An R, Cassin J, Joseph J, Mi R, Wang C, Zhong C, Jin SG, Pfeifer GP, Bellacosa A, et al. An Intrinsic Epigenetic Barrier for Functional Axon Regeneration. Neuron. 2017; 94:337–346. e336. [PubMed: 28426967]

Weng YL, An R, Shin J, Song H, Ming GL. DNA modifications and neurological disorders. Neurotherapeutics : the journal of the American Society for Experimental NeuroTherapeutics. 2013; 10:556–567. [PubMed: 24150811]

Weng YL, Joseph J, An R, Song H, Ming GL. Epigenetic regulation of axonal regenerative capacity. Epigenomics. 2016; 8:1429–1442. [PubMed: 27642866]

Widagdo J, Zhao QY, Kempen MJ, Tan MC, Ratnu VS, Wei W, Leighton L, Spadaro PA, Edson J, Anggono V, et al. Experience-Dependent Accumulation of N6-Methyladenosine in the Prefrontal Cortex Is Associated with Memory Processes in Mice. J Neurosci. 2016; 36:6771–6777. [PubMed: 27335407]

Wong JK, Zou H. Reshaping the chromatin landscape after spinal cord injury. Front Biol (Beijing). 2014; 9:356–366. [PubMed: 25554728]

Wright MC, Mi R, Connor E, Reed N, Vyas A, Alspalter M, Coppola G, Geschwind DH, Brushart TM, Hoke A. Novel roles for osteopontin and clusterin in peripheral motor and sensory axon regeneration. J Neurosci. 2014; 34:1689–1700. [PubMed: 24478351]

Yao B, Christian KM, He C, Jin P, Ming GL, Song H. Epigenetic mechanisms in neurogenesis. Nat Rev Neurosci. 2016; 17:537–549. [PubMed: 27334043]

Yoon KJ, Ringeling FR, Vissers C, Jacob F, Pokrass M, Jimenez-Cyrus D, Su Y, Kim NS, Zhu Y, Zheng L, et al. Temporal Control of Mammalian Cortical Neurogenesis by m(6)A Methylation. Cell. 2017; 171:877–889. e817. [PubMed: 28965759]

Yu J, Chen M, Huang H, Zhu J, Song H, Zhu J, Park J, Ji SJ. Dynamic m6A modification regulates local translation of mRNA in axons. Nucleic Acids Res. 2017

Zhang C, Chen Y, Sun B, Wang L, Yang Y, Ma D, Lv J, Heng J, Ding Y, Xue Y, et al. m6A modulates haematopoietic stem and progenitor cell specification. Nature. 2017; 549:273–276. [PubMed: 28869969]

Zhang C, Darnell RB. Mapping in vivo protein-RNA interactions at single-nucleotide resolution from HITS-CLIP data. Nature biotechnology. 2011; 29:607–614.

Zhao BS, Roundtree IA, He C. Post-transcriptional gene regulation by mRNA modifications. Nature reviews Molecular cell biology. 2017a; 18:31–42. [PubMed: 27808276]

Zhao BS, Wang X, Beadell AV, Lu Z, Shi H, Kuuspalu A, Ho RK, He C. m6A-dependent maternal mRNA clearance facilitates zebrafish maternal-to-zygotic transition. Nature. 2017b; 542:475–478. [PubMed: 28192787]

Zheng G, Dahl JA, Niu Y, Fedorcsak P, Huang CM, Li CJ, Vagbo CB, Shi Y, Wang WL, Song SH, et al. ALKBH5 is a mammalian RNA demethylase that impacts RNA metabolism and mouse fertility. Mol Cell. 2013; 49:18–29. [PubMed: 23177736]

Zhou J, Wan J, Gao X, Zhang X, Jaffrey SR, Qian SB. Dynamic m(6)A mRNA methylation directs translational control of heat shock response. Nature. 2015; 526:591–594. [PubMed: 26458103]

HIGHLIGHTS

- PNS nerve injury elevates m^6A-tagged mRNA encoding RAGs and translational machinery
- PNS nerve injury induces dynamic changes in the m^6A landscape of adult DRGs
- m^6A tagging promotes injury-induced global de novo protein synthesis in adult DRGs
- m^6A signaling is required for robust axon regeneration in adult PNS and CNS

One sentence summary

m^6A methylation promotes axon regeneration\

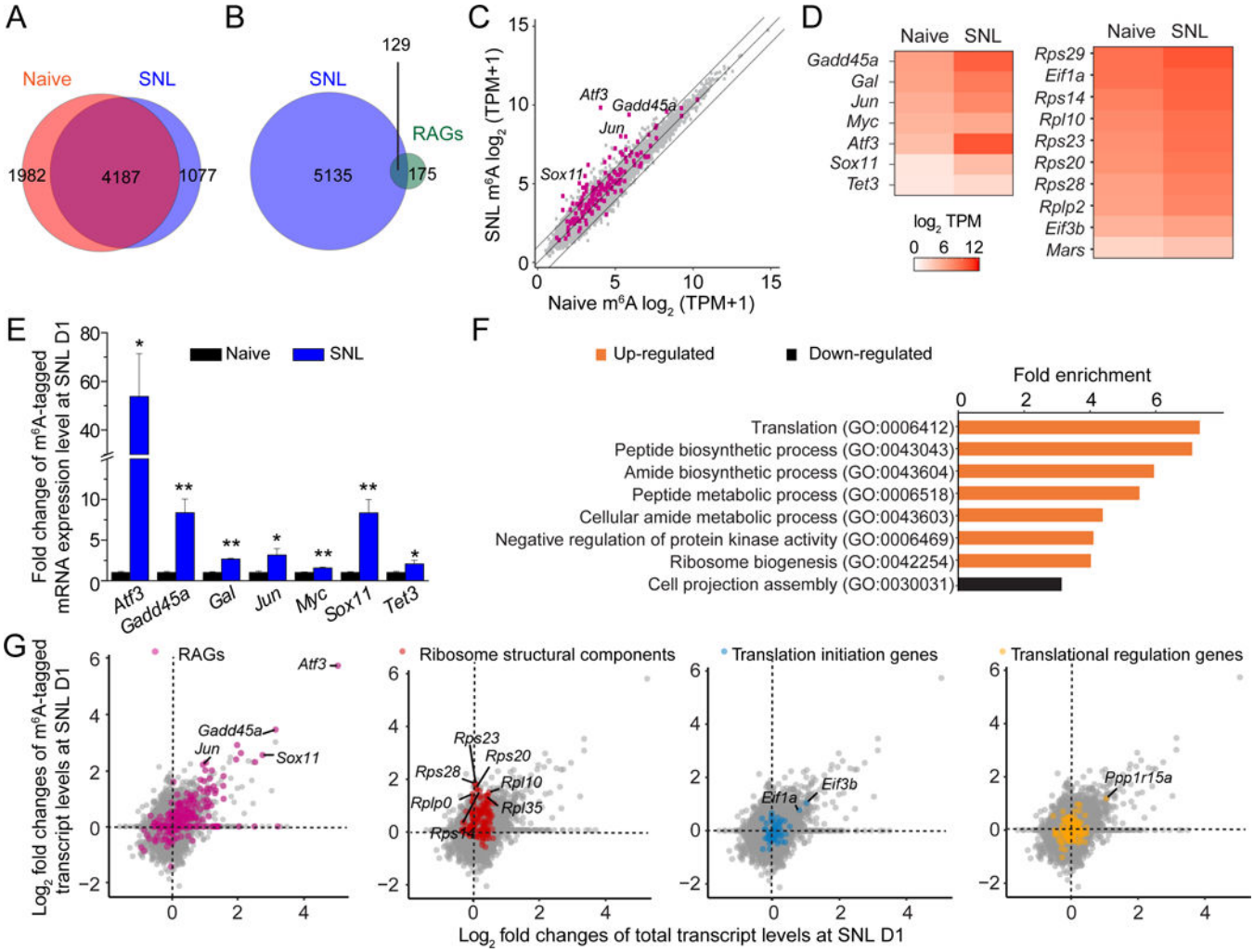

Figure 1. SNL upregulates levels of m^{6}A-tagged mRNAs encoding RAGs and protein translation machinery in adult DRGs in vivo

(**A**) Venn diagram of m^{6}A-tagged transcripts identified by m^{6}A-SMART-seq in adult mouse DRGs under naïve and SNL D1 conditions.

(**B**) Venn diagram of all m^{6}A-tagged genes at SNL D1 and known RAGs.

(**C**) Scatter plot of expression levels of m^{6}A-tagged transcripts under naïve and SNL D1 conditions. Lines indicate 2 fold differences and RAGs are indicated by magenta dots.

(**D**) Heatmap diagrams of the m^{6}A transcript levels under naïve and SNL D1 conditions for a select group of RAGs and genes related to protein translation functions.

(**E**) m^{6}A-MeRIP Q-PCR validation of differential m^{6}A transcript levels under naïve and SNL D1 conditions for selected RAGs. Values are normalized to the naïve condition and represent mean ± SEM (n = 3 experimental replications from 6 animals; *P < 0.05; **P < 0.01; t-test).

(**F**) GO enrichment analyses of the top 400 genes with increased m^{6}A-tagged transcript levels (orange) and the top 400 genes with decreased m^{6}A-tagged transcript levels (black) at SNL D1.

(**G**) Scatter plots of $\log_2$ fold changes of m^6A-tagged and total transcript levels between naïve and SNL D1 conditions. Subsets of genes are labeled with different colors in the same plot: RAGs (magenta), ribosomal subunit-related genes (red), translation initiation-related genes (blue), and translation regulation-related genes (yellow).
See also Figure S1.

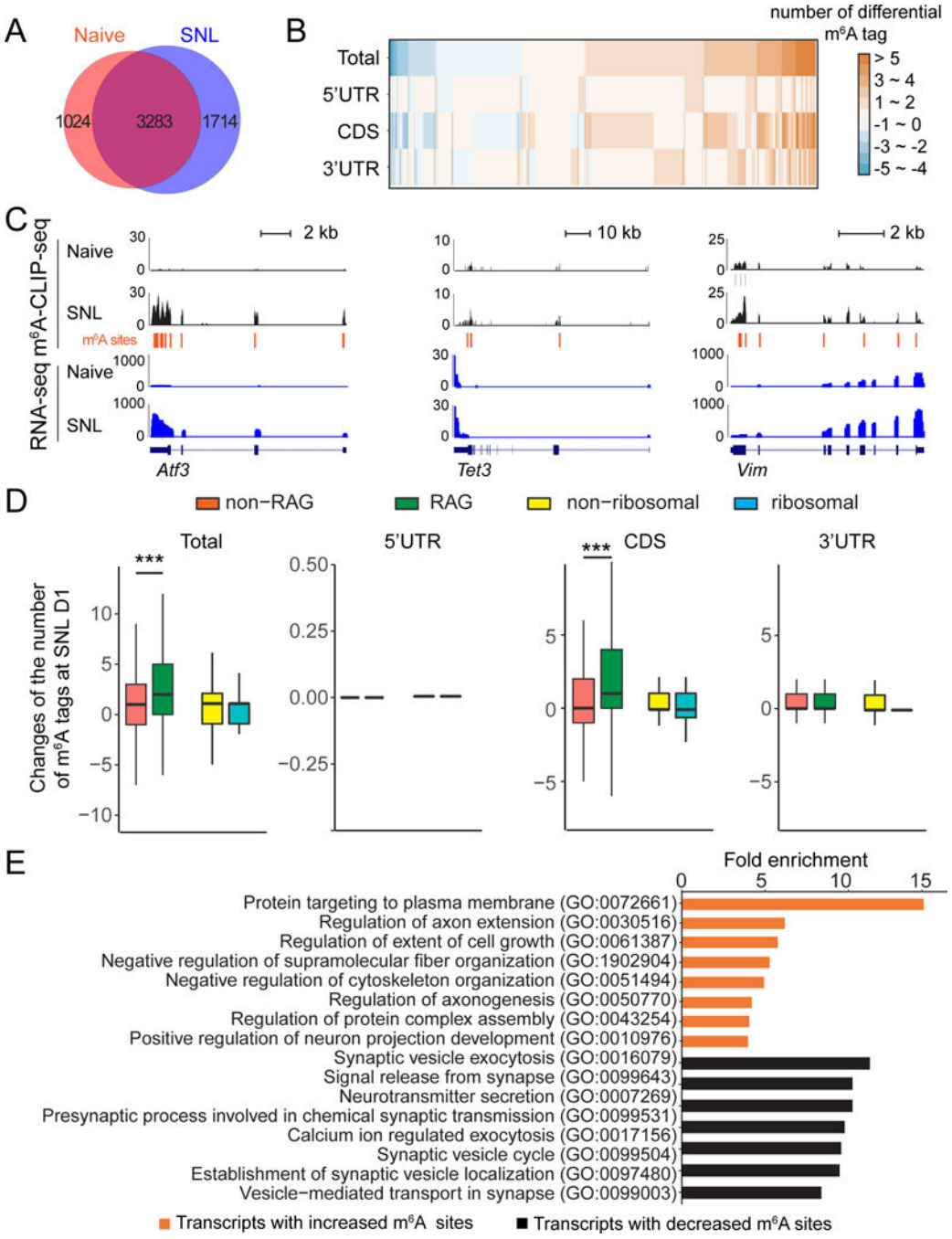

Figure 2. SNL modifies the m^{6}A landscape of transcriptomes of adult mouse DRGs in vivo

(**A**) Venn diagram of m^{6}A tagged-transcripts identified by m^{6}A-CLIP-SMART-seq in adult mouse DRGs under naïve and SNL D1 conditions.

(**B**) Dynamic changes of m^{6}A sites in transcripts from adult DRGs at SNL D1. Cn8ghanges of m^{6}A sites are plotted for the whole transcript (total) and in different sub-transcript regions (5′ UTR, CDS, and 3′ UTR). CDS: coding sequence region.

(**C**) m^{6}A-CLIP-SMART-seq examples for multiple RAGs. Shown are sample tracks for both m^{6}A-CLIP-seq (top panels) and RNA-seq (bottom panels). CLIP unique tag coverage is shown in black, and m^{6}A sites are indicated with vertical lines.
(**D**) Comparison of dynamic m^{6}A sites between RAGs and non-RAGs, and between transcripts encoding ribosomal subunit-related and non-ribosomal subunit-related proteins, in different transcript regions (total, 5′ UTR, CDS, and 3′ UTR) under naïve and SNL D1 conditions. Values represent mean differential m^{6}A tag numbers (n = 154 RAGs and 5,867 non RAGs; n = 55 ribosomal subunit-related and 5,966 non-ribosomal subunit-related genes; ***$P < 0.001$; one-way ANOVA with Tukey's post hoc test).
(**E**) GO enrichment analyses of transcripts with differential m^{6}A sites at SNL D1.
See also Figure S2.

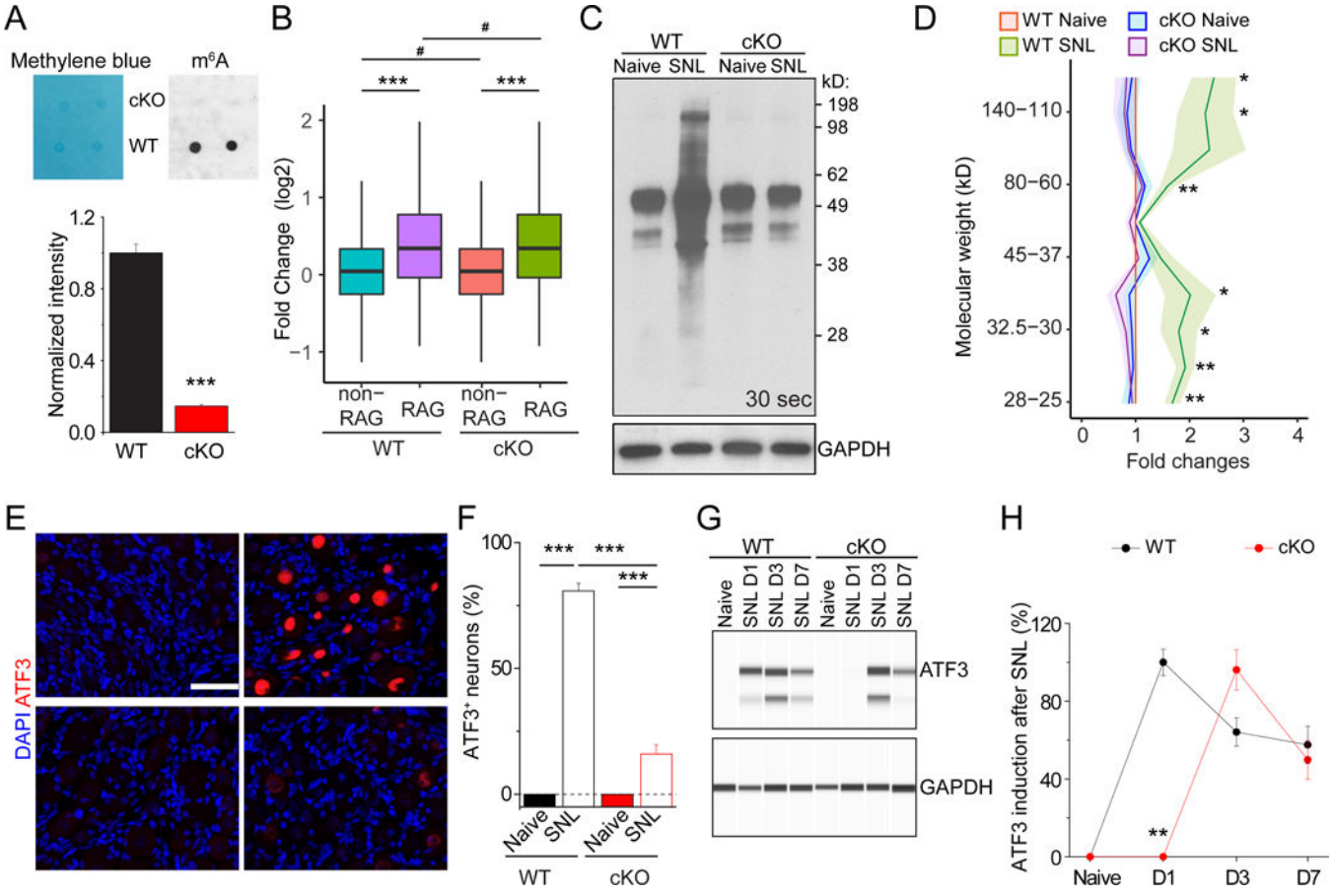

Figure 3. *Mettl14* deletion attenuates SNL-induced global protein translation and ATF3 protein expression in the adult DRG

(**A**) m^{6}A dot-blot showing diminished m^{6}A levels in mRNA from DRGs of adult *Syn-Cre;Mettl14* cKO mice. Methylene blue was used to assess the equal loading of mRNA. Representative images (top panel) and quantification (bottom panel) are shown. Values represent mean ± SEM (n = 2 animals per group; ***$P < 0.001$; two-way ANOVA).

(**B**) Box plots depicting the fold changes of the gene expression level between RAGs and non-RAGs after injury in WT and *Mettl14* cKO DRGs. Each box shows the first quartile, median, and third quartile (***$P < 0.001$; $^{\#}P > 0.05$; one-way ANOVA with Tukey's post hoc test).

(**C-D**) SUnSET analysis of new protein synthesis in adult L4/5 DRGs of WT and *Mettl14* cKO mice. De novo synthesized proteins were pulse-chase labeled for one hour after injection of puromycin at SNL D1. Western blot of DRG lysates were performed for different conditions. GAPDH was used as the loading control. Representative images (**C**) and quantification (**D**) are shown. Values are normalized to the WT naïve condition and plots represent ranges of mean ± SEM (n = 4 animals; **$P < 0.01$; *$P < 0.05$; two-way ANOVA). See Figure S3E for images from different exposures of the same Western blot example.

(**E-F**) Assessment of ATF3 induction in WT and *Mettl14* cKO DRGs at SNL D1. Sample images of ATF3 immunostaining (**E**) and quantification (**F**) are shown. Scale bars: 50 μm. Values represent mean ± SEM (n = 4 animals; ***$P < 0.001$; two-way ANOVA).

(**G-H**) Time-course analysis of ATF3 induction in WT and *Mettl14* cKO adult DRGs. Immunoassay of DRG protein lysates were performed by capillary electrophoresis. GAPDH was used as the loading control. Sample images of blots (**G**) and quantification (**H**) are shown. Values represent mean ± SEM (n = 3 animals; $^{**}P < 0.01$; two-way ANOVA). See also Figure S3.

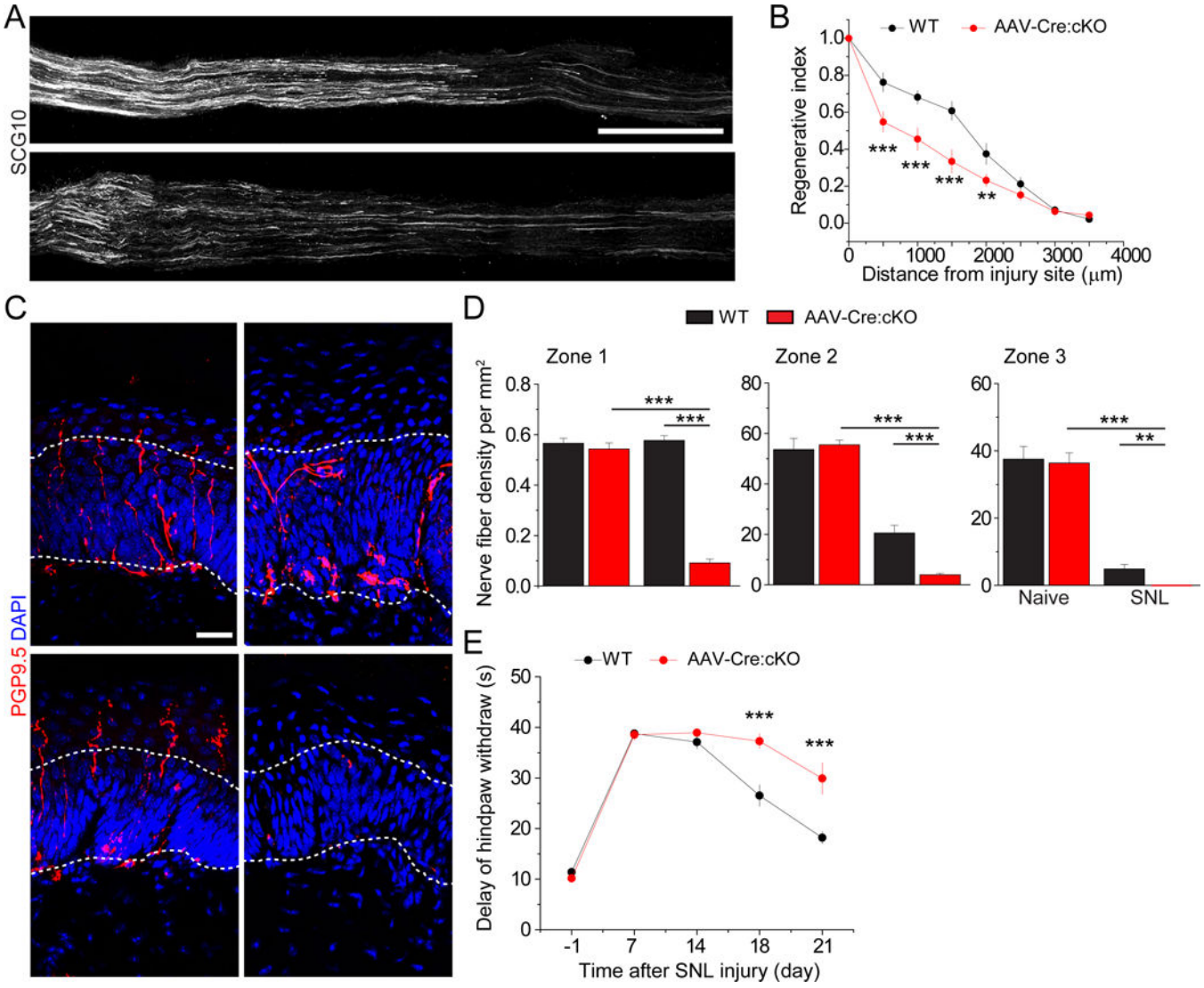

Figure 4. *Mettl14* deletion attenuates functional axon regeneration of adult DRG neurons in vivo

(**A-B**) Analysis of regeneration of sensory axons by SCG10 immunostaining at SNL D3 in adult WT and *Mettl14*$^{f/f}$ mice upon intrathecal injection of AAV2/9 to express Cre. Sample images of regenerating sensory axons identified by SCG10 (**A**; scale bar: 1 mm) and quantification (**B**) are shown. SCG10 immunofluorescence intensity was measured at different distal distances and normalized to that at 1 mm before the lesion site as the regenerative index. Values represent mean ± SEM (n = 8 animals for WT and 10 animals for AAV-Cre;*Mettl14* cKO; ***$P < 0.001$; **$P < 0.01$; two-way ANOVA).

(**C-D**) Assay for re-innervation of the hindpaw epidermal area by regenerating sensory axons. Sample images of cross sections of hindpaw glabrous skin of WT and AAV-Cre;*Mettl14* cKO mice immunostained with the pan neuronal marker PGP9.5 are shown (**C**). The dotted line indicates the border between dermis and epidermis. Scale bar: 20 μm. Also shown are quantifications of the number of intra-epidermal nerve fibers in a 1 mm segment of different epidermal areas (**D**). Values represent mean ± SEM (n = 5 animals per group; ***$P < 0.001$; **$P < 0.01$; two-way ANOVA).

(**E**) Assessment of thermal sensory recovery after SNL in WT and AAV-Cre;*Mettl14* cKO mice. Values represent mean ± SEM (n = 10 animals per group; ***$P < 0.001$; two-way ANOVA).

See also Figure S4.

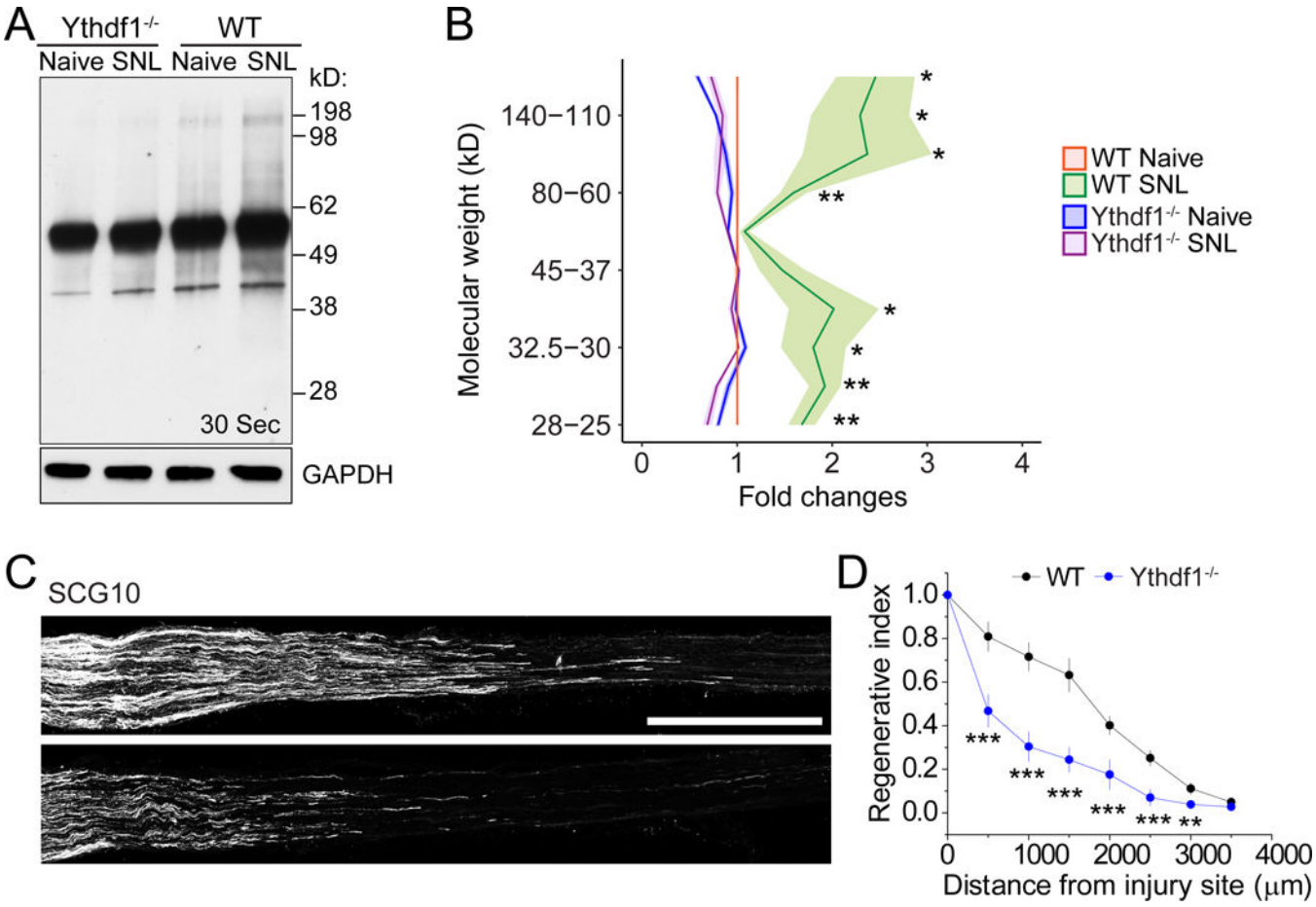

Figure 5. YTHDF1 is required for injury-induced global de novo protein synthesis and robust axon regeneration of adult DRG neurons

(**A-B**) SUnSET analysis of new protein synthesis in adult L4/5 DRGs of WT and *Ythdf1* KO mice. De novo synthesized proteins were pulse-chase labeled for one hour after injection of puromycin at SNL D1. Western blot of DRG lysates were performed for different conditions. GAPDH was used as the loading control. Representative images (**A**) and quantification (**B**) are shown. Values are normalized to WT naïve conditions and plots represent ranges of mean ± SEM (n = 3 for WT and *Ythdf1* KO each; ***$P < 0.01$; **$P < 0.01$; two-way ANOVA). See Figure S5C for images from different exposures of the same Western blot example.

(**C-D**) Analysis of regeneration of sensory axons by SCG10 immunostaining at SNL D3 in adult WT and *Ythdf1* KO mice. Sample images of regenerating sensory axons identified by SCG10 (**C**; scale bar: 1 mm) and quantification (**D**) are shown. SCG10 immunofluorescence intensity was measured at different distal distances and normalized to the level 1 mm before the lesion site as the regenerative index. Values represent mean ± SEM (n = 7 animals for WT and 6 animals for *Ythdf1* KO mice; ***$P < 0.001$; **$P < 0.01$; two-way ANOVA). See also Figure S5.

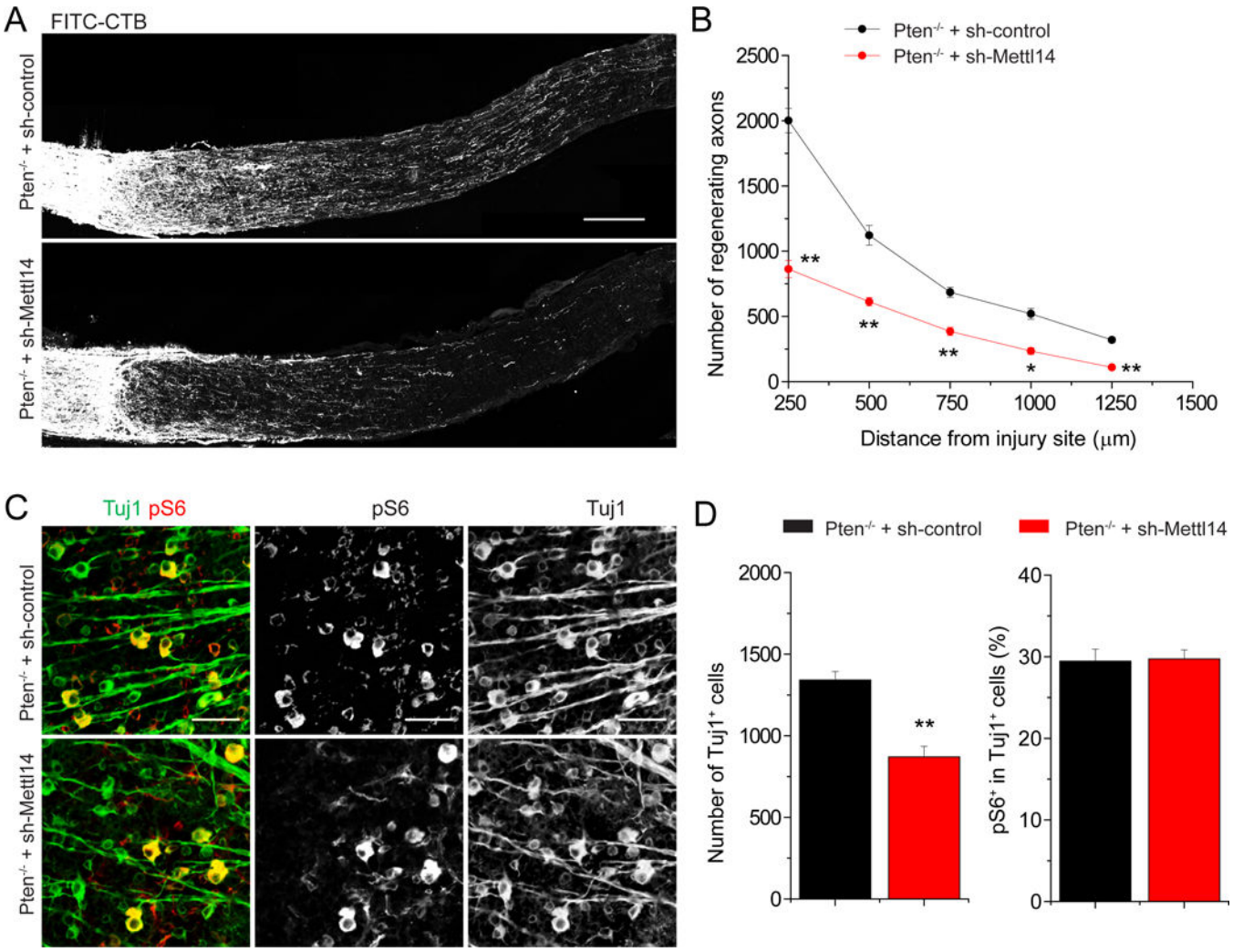

Figure 6. Mettl14 is required for robust *Pten* deletion-induced axonal regeneration of retinal ganglion neurons in the adult mouse CNS

Adult *Pten*$^{f/f}$ mice were co-injected with AAV-Cre and AAV-shRNA-control or AAV-shRNA-Mettl14. Optic nerve was crushed 4 weeks after AAV injection and RGC axons were traced by fluorescence conjugated cholera toxin B (FITC-CTB) 2 weeks later. Shown are sample images of sections of optic nerve containing FITC-CTB-labeled axons (**A**; scale bar: 200 μm) and quantification of numbers of regenerating axons at different distances from the injury site (**B**). Values represent mean + SEM (n = 5 animals per group; ** $P < 0.01$; * $P < 0.05$; ANOVA followed by Fisher's LSD). Also shown are sample images of whole-mount retina with Tuj1 (green) and pS6 (red) immunostaining (**C**; scale bar: 50 μm) and quantification of densities of Tuj1$^+$ RGCs and percentages of Tuj1$^+$ RGCs expressing pS6. Values represent mean + SEM (n = 5 animals per each group; ** $P < 0.01$; Student's t test). See also Figure S6.